

1
2
3
4
5
6
7 **A More Transparent Infrared Window**
8
9

10
11
12
13 Eli J. Mlawer (mlawer@aer.com)¹
14 Jeana Mascio¹
15 David D. Turner²
16 Vivienne E. Payne³
17 Connor J. Flynn⁴
18 Robert Pincus⁵
19
20
21

22 Affiliations

23 ¹Atmospheric and Environmental Research, Lexington, Massachusetts

24 ²NOAA/Global Systems Laboratory, Boulder, Colorado

25 ³Jet Propulsion Laboratory, California Institute of Technology, Pasadena, California

26 ⁴University of Oklahoma School of Meteorology, Norman, Oklahoma

27 ⁵Lamont-Doherty Earth Observatory, Columbia University, Palisades, New York
28
29

30 Key points:

- 31
- 32 • Analysis of ground-based radiance observations indicates that the infrared window region is more transparent than had been thought
 - 33 • The derived water vapor self continuum is 10-30% weaker than previously thought, while
 - 34 the foreign continuum is substantially stronger
 - 35 • The revised H₂O continuum results in a 5-10% increase in climate feedback and a large
 - 36 change to the radiative budget for moist atmospheres
- 37
38

39 **Abstract**

40
41 The infrared window region (780-1250 cm⁻¹, 12.8 to 8.0 μm) is of great importance to Earth's
42 climate due to its high transparency and thermal energy. We present here a new investigation of
43 the transparency of this spectral region based on observations by interferometers of downwelling
44 surface radiance at two DOE Atmospheric Radiation Measurement program sites. We focus on the
45 dominant source of absorption in this region, the water vapor continuum, and derive updated
46 values of spectral absorption coefficients for both the self and foreign continua. Our results show
47 that the self continuum is too strong in the previous version of Mlawer-Tobin_Clough-Kneizys-
48 Davies (MT_CKD) water vapor continuum model, a result that is consistent with other recent
49 analyses, while the foreign continuum is too weak in MT_CKD. In general, the weaker self
50 continuum derived in this study results in an overall increase in atmospheric transparency in the
51 window, although in atmospheres with low amounts of water vapor the transparency may slightly
52 decrease due to the increase in foreign continuum absorption. These continuum changes lead to a
53 significant decrease in downwelling longwave flux at the surface for moist atmospheres and a
54 modest increase in outgoing longwave radiation. The increased fraction of surface-leaving
55 radiation that escapes to space leads to a notable increase (~5-10%) in climate feedback, implying
56 that climate simulations that use the new infrared window continuum will show somewhat less
57 warming than before. This study also points out the possibly important role that aerosol absorption
58 may play in the longwave radiative budget.

59
60 **Plain Language Summary**

61 The spectral region in the infrared from 780-1250 cm⁻¹ (12.8 to 8.0 μm) is referred to as a window
62 due to its transparency – in this region, thermal radiation emitted by the surface can pass relatively
63 unimpeded through the atmosphere, allowing Earth to cool. The limited amount of atmospheric
64 absorption that does occur in this region is primarily due to water vapor, in particular an absorption
65 mechanism termed the water vapor continuum. The strength of water vapor continuum absorption
66 in the infrared window therefore has important consequences for Earth's climate. This study
67 provides a new evaluation of water vapor continuum absorption in the infrared window from an
68 analysis of spectrally resolved measurements of downwelling surface radiances. Our results
69 indicate that for most atmospheres the strength of water vapor continuum absorption is less than
70 had been previously thought due to reduced absorption related to the interactions of water vapor
71 molecules with other water vapor molecules, i.e. the water vapor self continuum. The derived
72 water vapor continuum changes allow the Earth to cool ~5-10% better than had previously been
73 thought, and climate simulations that use the revised infrared window continuum will show
74 somewhat less warming than before.

75 **1. Introduction**

76 Atmospheric absorption in the infrared window (780-1250 cm⁻¹, 12.8 to 8.0 μm) plays an important
77 role in Earth’s radiation budget and climate, a consequence of this spectral region’s high thermal
78 energy, relative transparency, and the properties of its most important source of absorption, the
79 water vapor self continuum. The self continuum is a weak absorber under typical atmospheric
80 conditions, but its strength increases quadratically with water vapor abundance so under moist
81 conditions self continuum absorption can result in significant atmospheric opacity. The importance
82 of the infrared window region and the dominance of the water vapor self continuum absorption in
83 this region make it imperative that the properties of this absorber be known with high certainty so
84 that atmospheric applications that depend on window absorption can be regarded with confidence.
85 This study presents the result of a new radiative closure analysis (Mlawer and Turner, 2016;
86 Shepherd et al., 2003) of water vapor continuum absorption in the infrared window.

87
88 Longwave radiation that escapes to space (outgoing longwave radiation or OLR) is a critical
89 component of the Earth’s radiation budget. Most of the thermal radiation emitted by the Earth’s
90 surface is absorbed by the atmosphere, which then emits thermal radiation at its own temperature,
91 which typically is less than the surface temperature. An exception to this general behavior occurs
92 in spectral regions that are relatively transparent in clear skies, in which the warm radiation emitted
93 by the surface is only slightly attenuated and therefore escapes the atmosphere. These spectral
94 regions are called “windows” -- the most important with respect to Earth’s thermal radiation is the
95 infrared window. For six reference atmospheres, Table 1 shows the total surface flux emitted by
96 the surface, the surface flux in spectral regions in which the total vertical optical depth is less than
97 1, and the fraction of this “transparent-region” flux that is in the infrared window. These values
98 indicate that only a limited amount of the surface flux has the potential to escape to space, and a
99 large fraction of that amount is in the infrared window.

100
101 As has been shown in recent studies (e.g. Seeley and Jeevanjee, 2021; Jeevanjee et al., 2021; Koll
102 and Cronin, 2018), the infrared window plays a crucial role in climate and climate feedback. These
103 studies show that at typical current surface temperatures the infrared window is the primary
104 spectral region in which the radiation that escapes to space can change as the planet adjusts to an
105 energy imbalance, such as is being currently precipitated by anthropogenic increases in greenhouse

Reference atmosphere	Precipitable water vapor (cm)	Total surface flux (W/m ²)	Surface flux for OD < 1	Fraction of OD < 1 flux in IR window
Tropical	4.1	451.62	155.56	0.98
Midlatitude summer	2.9	420.03	171.19	0.97
US standard	1.4	387.41	199.71	0.85
Subarctic summer	2.1	382.15	158.48	0.96
Midlatitude winter	0.9	309.34	178.37	0.74
Subarctic winter	0.4	247.16	165.62	0.60

106
107
108
109
110
111
112

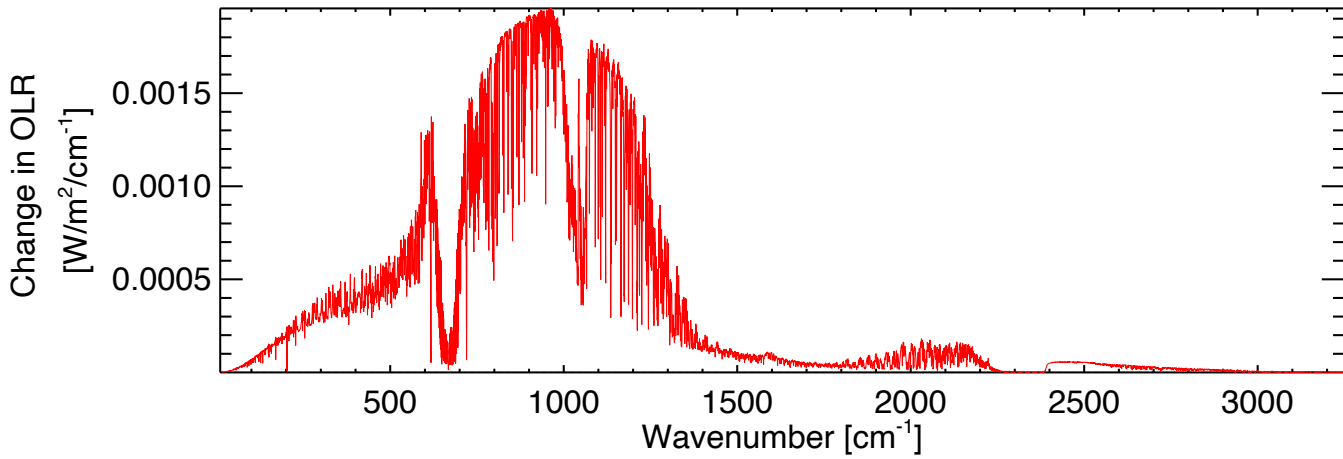
Table 1. For six reference atmospheres: total upwelling longwave flux at the surface, precipitable water vapor, upwelling flux in the portion of the longwave that are sufficiently transparent (vertical optical depth < 1) so that a significant fraction of the radiation emitted by the surface reaches the top of the atmosphere, and the fraction of the transparent-region surface flux that is in the IR window region. Surface emissivity is assumed to be unity.

113 gases. As an illustration of this effect, the change in OLR for a simplistic version of current
114 warming is shown in Fig. 1: a 1 K increase in tropospheric temperatures is applied to a baseline
115 profile, with relative humidity values and the tropospheric column amounts of all other species are
116 left unchanged in the perturbed profile. The results indicate that the change in OLR is primarily in
117 the infrared window.

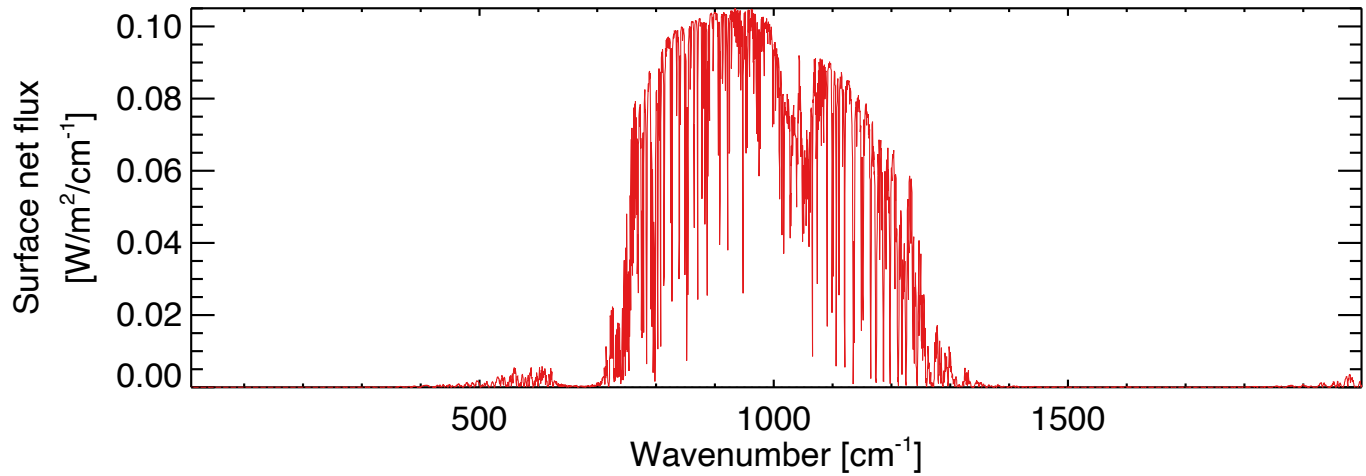
118
119 The infrared window is also critically important with respect to downwelling and net flux at the
120 surface. In opaque spectral regions, the downwelling flux arriving at the surface typically is
121 emitted at a temperature close to the surface temperature, resulting in a small net flux at the surface.
122 As shown in Fig. 2, in the infrared window emitted downwelling radiation that reaches the surface
123 is significantly smaller than the upwelling radiation, leading to a large net flux. The net flux
124 divergence, which drives radiative cooling and heating, is also of unique importance in this
125 window. The quadratic dependence on water vapor abundance of the self continuum optical depths
126 leads to large relative gradients in optical depth in the lower atmosphere, and therefore large
127 radiative flux divergences. Due to this effect, for moist atmospheres around 75% of the longwave
128 cooling rate near the surface occurs in the window (Mlawer et al., 1997).

129
130 Section 2 provides background information on water vapor continuum absorption in the infrared
131 window. Section 3 presents information about the radiometric measurements used in this study,
132 the radiative transfer model calculations used to compare with these measurements, and details
133 about how the atmospheric properties used in the calculations were obtained. Section 4 contains
134 details about how the measurement-calculation differences were analyzed and then utilized to
135 derive self and foreign continuum coefficients in the infrared window, as well as a specification of
136 the self continuum temperature dependence. Section 5 compares the derived results to results
137 obtained in previous studies and section 6 discusses the impact of the new window water vapor
138 continuum results on atmospheric applications. Section 7 provides a summary and discussion.

139
140 **2. The Water Vapor Continuum in the Infrared Window**
141 We provide here background information concerning our understanding of water vapor continuum
142 absorption in the infrared window and its development over the last several decades, including its
143 treatment in the Mlawer-Tobin_Clough-Kneizys-Davies (MT_CKD) water vapor continuum



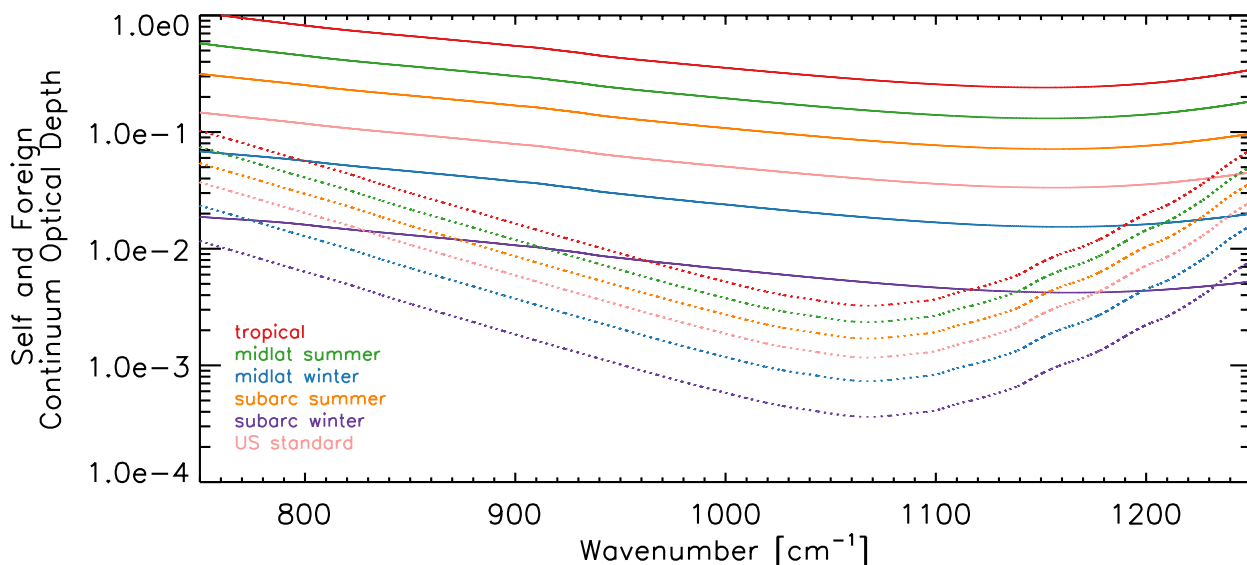
144 **Fig. 1.** Change in OLR due to a 1 K increase in tropospheric temperatures in the mid-latitude summer
 145 atmosphere with relative humidity left unchanged.



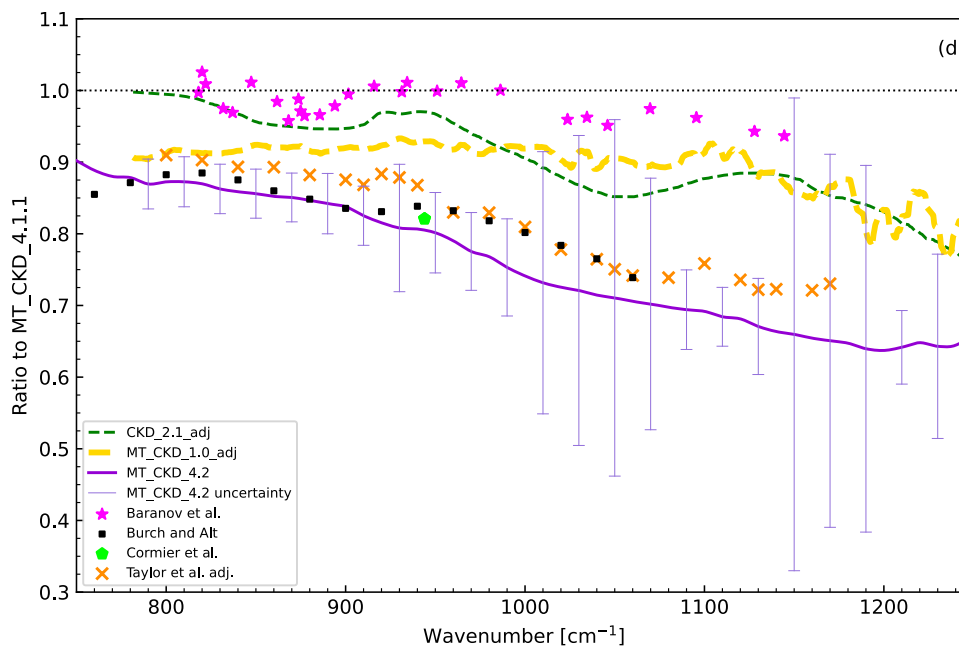
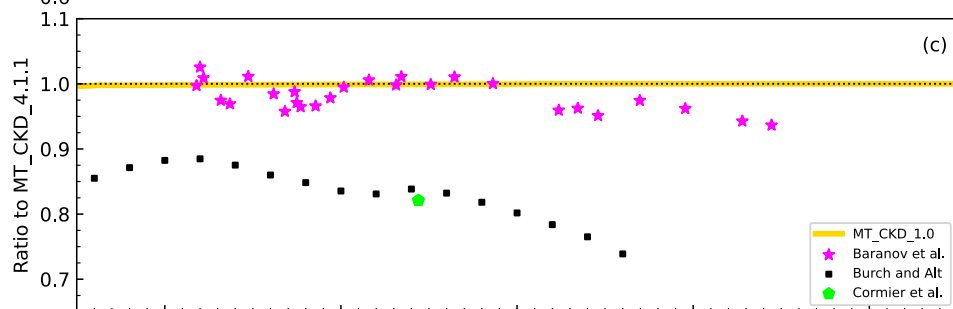
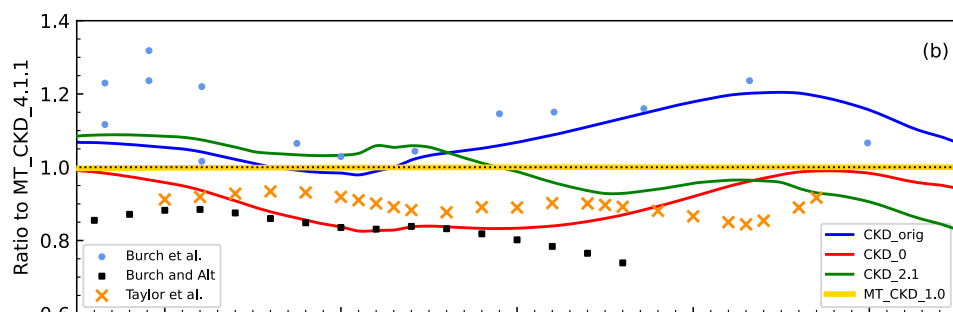
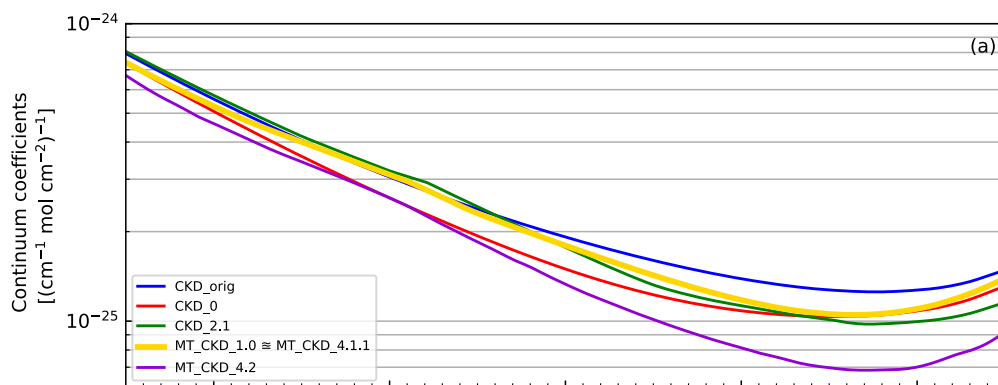
146 **Figure 2.** Magnitude of longwave surface net flux for the mid-latitude summer atmosphere.
 147

148 model (Mlawer et al., 2023; Mlawer et al., 2012), the primary source used in the community to
 149 specify water vapor continuum absorption in this spectral region. For reference, self and foreign
 150 continuum optical depths from the current version of MT_CKD (v4.1.1) are shown in Fig. 3 for
 151 six reference profiles. In recent years, self continuum absorption in the infrared window had been
 152 thought to be fairly well known, with the most recent laboratory measurement of the self
 153 continuum in this region (Baranov et al., 2008) agreeing well at atmospheric temperatures with the
 154 MT_CKD continuum model, which is based on a recent field study (Turner et al., 2004). However,
 155 a review of studies of the self continuum absorption in this region over the last several decades
 156 shows cracks in this consensus.

157
 158 The specification of the window self continuum in the original version of the Clough-Kneizys-
 159 Davies (CKD) continuum model (see Figs. 3 and 5 of Clough et al., 1989 – Note: the caption of
 160 Fig. 3 in Clough et al., 1989, erroneously states that the broadening pressure is 1013 mb, when it
 161 actually is 26.7 mb), the predecessor to the MT_CKD model, was based on the laboratory results
 162 of Burch (1982). These CKD values can be seen in Fig. 4a and are also shown along with the
 163 Burch (1982) measurements in Fig. 4b. Burch and collaborators subsequently significantly revised
 164 their experimental values, with the new lower continuum absorption coefficients (also shown in
 165 Fig. 4b) ascribed to “minor changes in experimental techniques employed in the recent work”
 166 (Burch and Alt, 1984). These improved experimental values were used as the basis for an updated



167 **Fig 3.** Optical depths due to the MT_CKD_4.1.1 water vapor self (solid) and foreign (dotted) continua for
 168 a vertical path for six reference atmospheric profiles.

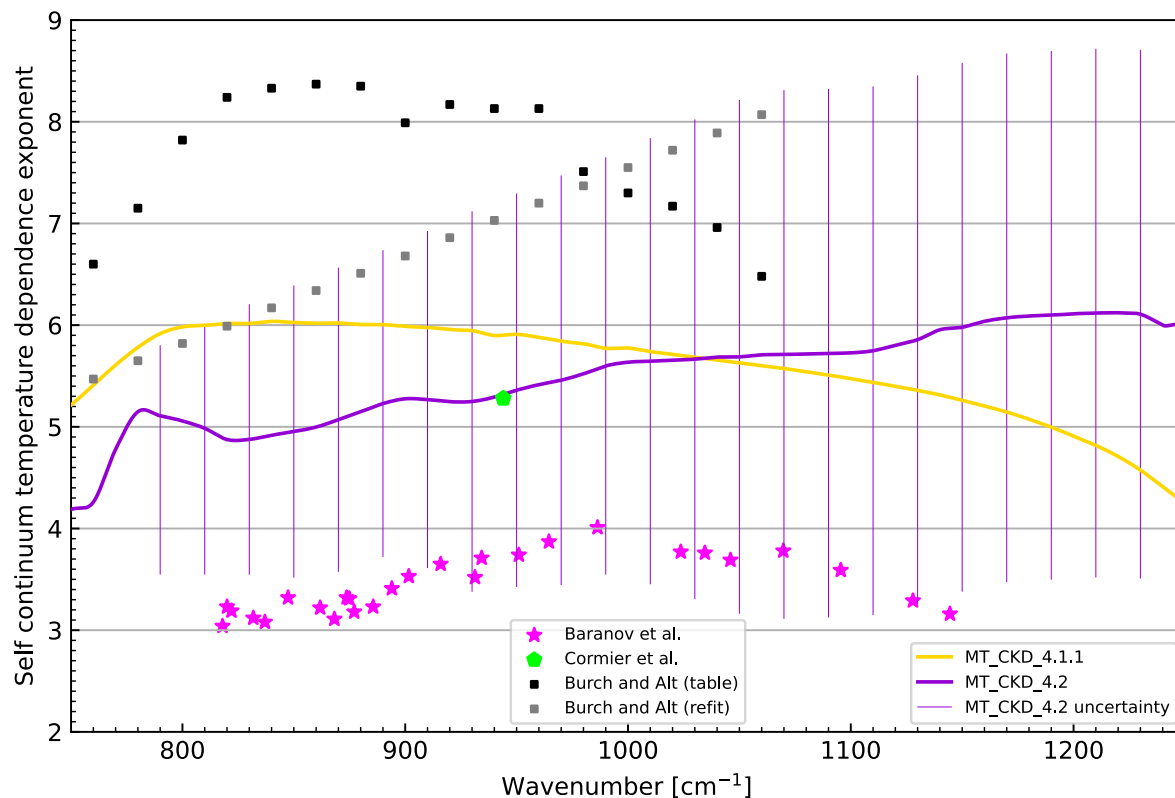


170 **Fig. 4.** Various perspectives on the water vapor self continuum in the infrared window. (a) Water vapor self
171 continuum coefficients for five versions of the CKD and MT_CKD continuum. The yellow curve is the self
172 continuum at the beginning of this study, MT_CKD_4.1.1, and the purple curve shows the result of this
173 study, MT_CKD_4.2; (b) Overview of the self continuum in ~2004. Shown as ratios with respect to
174 MT_CKD_4.1.1 are several previous versions of CKD and MT_CKD as well as two sets of laboratory
175 measurements (blue circles and black squares) and the result from the Taylor et al. field campaign (orange
176 X's); (c) Key evaluations of the self continuum before this study are shown as ratios with respect to
177 MT_CKD_4.1.1; (d) Overview of the self continuum after this study. Shown as ratios with to
178 MT_CKD_4.1.1 are the most recent laboratory measurements from three groups (pink stars, black squares,
179 and green pentagon) and the results from three field studies (Taylor et al., 2003, orange X's; CKD_2.1
180 (green dashed curve), which was motivated by Westwater et al., 1995); MT_CKD_1.0 (yellow dashed
181 curve), which was motivated by Turner et al., 2004) that have been adjusted to account for a stronger foreign
182 continuum (as described in the text) than had been used in the respective original analyses. The purple curve
183 shows the significant decrease in the self continuum that is derived in this study, MT_CKD_4.2 – note that
184 in some regions the corresponding derived error (purple vertical lines with end caps) is significant.
185

186 version of the CKD model (CKD_0, see Fig. 7 of Clough et al., 1989). The next update of
187 consequence to the CKD window self continuum occurred about a decade later as a result of
188 analyses of Fourier transfer infrared (FTIR) spectrometer measurements in the tropics (Westwater
189 et al., 1995; Han et al., 1997), which resulted in an increase in the window self continuum in
190 version 2.1 of CKD (shown in Fig. 4a,b). A few years later, an analysis by Turner et al. (2004)
191 using measurements by the Atmospheric Emitted Radiance Interferometer (AERI; Knuteson et al.,
192 2004 a,b) deployed at the Southern Great Plains (SGP; Sisterson et al., 2016) site of Atmospheric
193 Radiation Measurement (ARM) program (Turner & Ellingson, 2016) demonstrated that the
194 window self continuum in CKD needed modification, which led to the values in this region adopted
195 in the first version of the MT_CKD continuum model, MT_CKD_1.0 (Mlawer et al., 2012), also
196 shown in Fig. 4. Fig. 4b also presents the results of a field study of the self continuum by Taylor
197 et al. (2003).

198
199 With respect to laboratory measurements of the window self continuum, there was a gap of almost
200 20 years between the measurements of Burch and subsequent studies. A 2005 laboratory study by
201 Cormier et al. supported a significantly lower continuum absorption coefficient than in
202 MT_CKD_1.0. These measurements were performed using the accurate cavity ring down
203 technique but were only at a single spectral point and contradicted the results from a study by the
204 same group (Cormier et al., 2002) a few years earlier. A subsequent laboratory study using an
205 FTIR (Baranov et al., 2008), mentioned above, showed good agreement with MT_CKD at typical
206 atmospheric temperatures, although significant disagreements were seen with respect to the
207 model's temperature dependence of the self continuum in this region (Fig. 5). The self continuum
208 coefficients derived in Baranov et al. (2008) are shown in Fig. 4c. Also shown in this figure are
209 the laboratory measurements by Burch (1982) – these measurements, and not those from Burch
210 and Alt (1984), were shown in Fig. 8 of Baranov et al. (2008), which drove home that there was
211 agreement between specifications of the window self continuum at room temperature (with the
212 exception of the Cormier et al., 2005, study). However, a conclusion that a consensus existed at
213 this time between laboratory and field studies of the window self continuum is flawed.

214
215 To see why, a closer consideration of window self continuum studies based on field measurements
216 is required. There is an important distinction between the window self continuum values based on
217



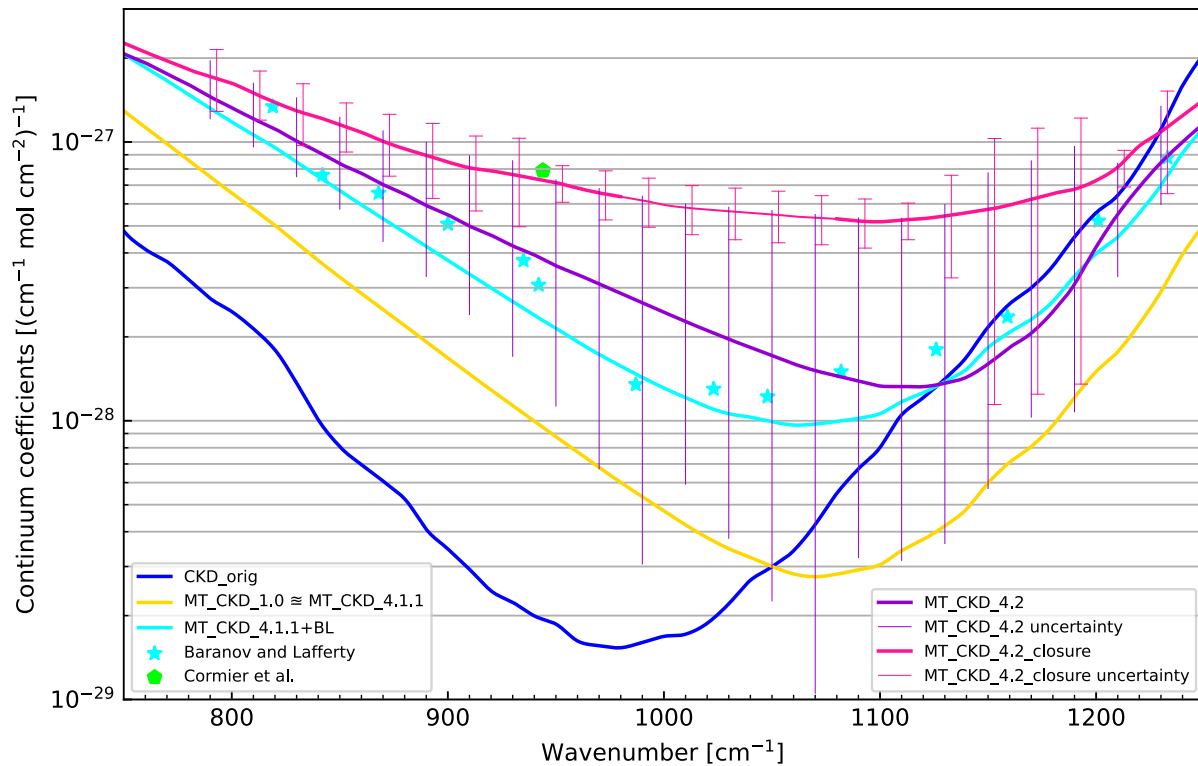
218 **Fig. 5.** The temperature exponent of self continuum coefficients from 750-1250 cm⁻¹ from several
 219 laboratory studies (various symbols), the previous version of MT_CKD, v4.1.1 \cong v1.0 (yellow curve), and
 220 the version derived in this study, MT_CKD_4.2 (purple curve), with estimated uncertainties shown in
 221 vertical purple lines without end caps.
 222

223 field studies (i.e. those that motivated the development of CKD_2.1 and MT_CKD_1.0, as shown
224 in Fig. 4b) and those based on laboratory studies (Fig. 4c). Laboratory studies utilize cells that
225 contain pure water vapor, while the atmospheric paths relevant to field studies are comprised of
226 mostly air (primarily nitrogen and oxygen) with a small fraction of water vapor. Therefore, field
227 studies have a dependence on the water vapor foreign continuum in the window, while laboratory
228 studies typically do not. Although the foreign continuum is much weaker than the self continuum
229 in the window (Fig. 3), significantly inaccurate values assumed for the foreign continuum can still
230 have an impact on the derived self continuum in analyses of field observations. Therefore, the
231 evolution of window foreign continuum values, while interesting in its own right given the
232 objectives of the current study, is also key to a proper understanding of past studies of window self
233 continuum absorption.

234

235 The original CKD foreign continuum values (Clough et al., 1989) in the window were based on
236 Burch (1982), which supported the conclusion that the foreign continuum was a very weak
237 absorber in this region (Fig. 6). A major increase in the window foreign continuum came about
238 with advent of MT_CKD (Mlawer et al., 2012), which resulted not from new foreign continuum
239 measurements in this region but rather as a consequence of constraining the model's derived line
240 shape parameters to fit the foreign continuum behavior from 500-750 cm^{-1} in its predecessor
241 version, CKD_v2.4.1. These increased MT_CKD foreign continuum coefficients in the window
242 were subsequently shown to be consistent with field observations by Turner et al. (2004). Even
243 with this increase, foreign continuum absorption in this region remained rather weak compared to
244 the self continuum. The laboratory measurement of Cormier et al. (2005) at 944 cm^{-1} , however,
245 supported a much higher level of foreign continuum absorption, and was followed by a more
246 extensive study (measurements at numerous points between 800-1250 cm^{-1}) by Baranov and
247 Lafferty (2012). As can be seen in Fig. 6, the Baranov and Lafferty (2012) study indicated that the
248 foreign continuum was ~2-4 times greater than MT_CKD_1.0, although the reported strength was
249 about half as large as specified in Cormier et al. (2005). Given the relative optical depths of the
250 window foreign and self continua shown in Fig. 3, assuming a 2-4 times larger foreign continuum
251 would have an appreciable effect on the self continuum absorption derived in a field study.

252



254 **Fig. 6.** Water vapor foreign continuum coefficients from 750-1250 cm^{-1} for the original version of the CKD
 255 model (blue curve), the current version of the MT_CKD model (v4.1.1, which is equivalent to
 256 MT_CKD_1.0, yellow curve), the laboratory results from Baranov and Lafferty (2012, cyan stars) and
 257 Cormier et al. (2005, green pentagon), and a version of MT_CKD (v4.1.1+BL, cyan curve) that was
 258 adjusted to be consistent with the Baranov and Lafferty (2012) results. The foreign continuum derived in
 259 this study, MT_CKD_4.2, is shown in purple, with associated uncertainty values shown with vertical lines
 260 without end caps. The pink curve shows the foreign continuum (MT_CKD_4.2_closure) needed to obtain
 261 radiative closure with the SGP observations used in this study. Error bars based on the SGP data set are
 262 pink vertical lines (slightly offset in the x-direction for clarity) with end caps.
 263

264 Given that the window foreign continuum derived in Baranov and Lafferty (2012) is much larger
265 than the corresponding foreign continuum values assumed in previous analyses of field
266 observations, it is instructive to understand to what extent the self continuum values derived in
267 previous field studies would have been affected had a stronger foreign continuum been utilized
268 instead in these studies. To evaluate this, we modify the current version of MT_CKD such that the
269 window foreign continuum coefficients are increased to be generally consistent with the Baranov
270 and Lafferty (2012) values. This modified foreign continuum version is shown as
271 MT_CKD_4.1.1+BL in Fig 6. We use this modified version to estimate (method described in
272 Appendix 1) the change in the self continuum values that would have been obtained in three prior
273 field studies had a greater foreign continuum been assumed rather than the values that actually
274 were used in these studies. These reconsidered self continuum values are shown in Fig. 4d as
275 MT_CKD_1.0_adj, CKD_2.1_adj, and Taylor_adj (which, respectively, are based off the studies
276 of Turner et al., 2004, Westwater et al., 1995/Han et al., 1997, and Taylor et al., 2003). We also
277 include on this figure the self continuum laboratory results of Cormier et al. (2005), Baranov et al.
278 (2008), and Burch and Alt (1984), which improved upon the previous measurements by the Burch
279 group.

280
281 The overall impression given by Fig. 4d is murkier than in Fig. 4c (or in Fig. 8 of Baranov et al.,
282 2008), but the observational evidence clearly allows the possibility that the window self continuum
283 is significantly weaker than in current MT_CKD. The diversity of values shown suggests,
284 however, that there is no consensus for the strength of the window self continuum. The main
285 motivation for this current study is to bring some clarity to this question of great importance.

286

287 **3. Elements of the Comparison**

288 Our analysis of water vapor continuum absorption in the infrared window is based on comparisons
289 between clear-sky radiance measurements by the AERI and corresponding calculations by the
290 Line-By-Line Radiative Transfer Model (LBLRTM; Clough et al., 2005) that utilize as input a
291 combination of in situ measurements, retrieved quantities, and model output to specify the
292 atmospheric properties in the radiating column above the AERI.

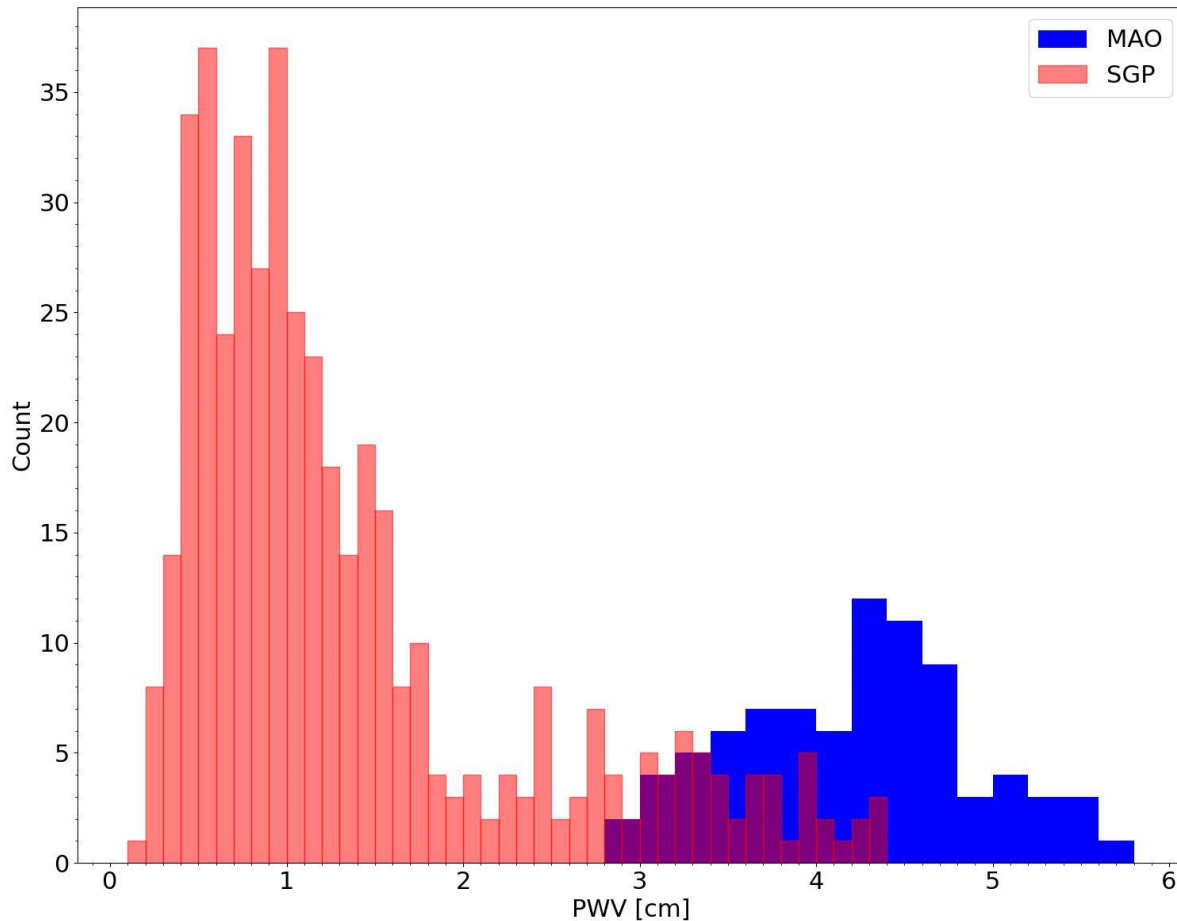
293

294 Our radiative closure analysis is based on observations taken at two sites operated by the ARM
295 program. The primary data set is more than two years of observations (March 2016 - October
296 2018) from the ARM SGP site, the world's largest and most extensive climate research facility.
297 The SGP site consists of in situ and remote-sensing instrument clusters and has been collecting
298 data since it was established in 1993. Also used in this study are observations from the ARM
299 Observations and Modeling of the Green Ocean Amazon (GoAmazon; Martin et al., 2016)
300 campaign (MAO), held from January 2014 through November 2015 in Manaus, Brazil, at an
301 altitude of about 50 meters. Due to MAO's tropical location the median PWV amount for the
302 profiles used in our analysis is far greater than for SGP (Fig. 7) and provide an excellent dataset
303 for validating the self and foreign continuum derived from SGP observations.

304

305 We provide here details about each of the three elements involved in this radiative closure study.

306



307 **Fig. 7.** Precipitable water vapor amounts for the cases used in this study.

308

309 **3.1 Radiometric Measurements**

310 The AERI, a Fourier transform infrared interferometer that was designed specifically for the ARM
 311 program (Turner et al., 2016), measures downwelling spectrally resolved infrared radiance from
 312 550-3000 cm^{-1} . A zenith-looking AERI, deployed at an altitude of 320 m, has been providing
 313 operational radiance measurements at SGP since 1995, observing radiances emitted downward by
 314 the atmosphere for a large range of water vapor column amounts (PWVs). It uses two detectors to
 315 have sensitivity to radiance in the 3.3 to 19 μm band, and the maximum optical path delay provides
 316 a spectral resolution of 0.5 cm^{-1} . The instrument regularly views two well-characterized
 317 blackbodies, which are operated at ambient temperature and 60 $^{\circ}\text{C}$, respectively. These blackbody
 318 observations, together with a correction for the detector's non-linearity, allows the instrument to
 319 measure downwelling spectral infrared radiance with a radiometric accuracy better than 1% of the
 320 ambient radiance. Additionally, a calibrated metrology laser and corrections for the finite field-of-

321 view of the instrument provides the spectral calibration for the observed radiance. Details on the
322 instrument and its calibration method are provided in Knuteson et al. (2004a, b).

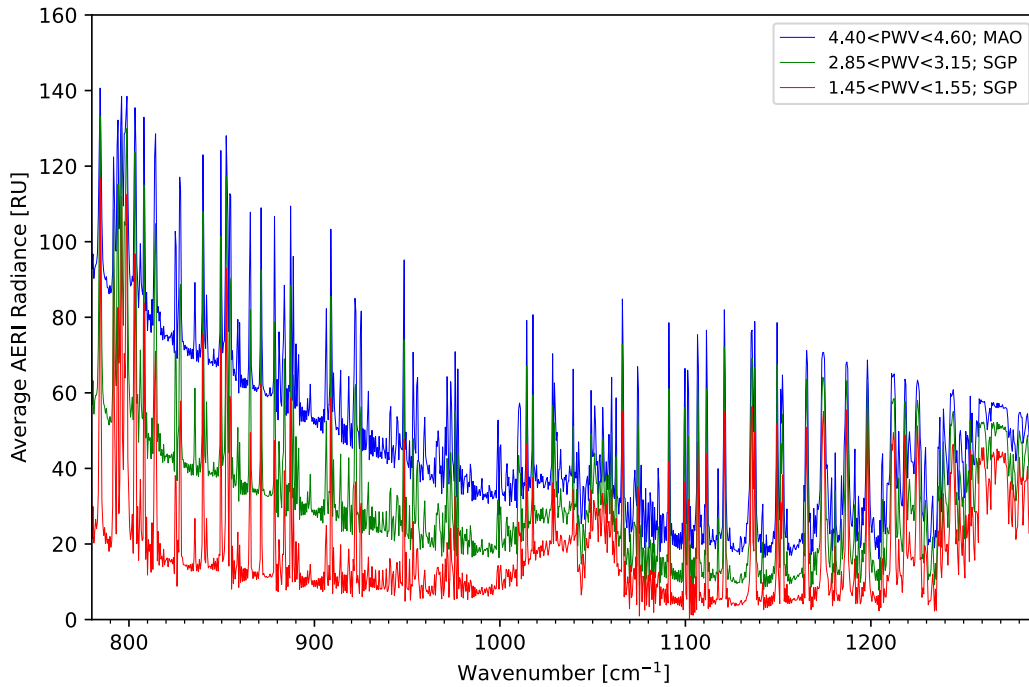
323
324 The signal observed from the sky is calibrated using the ambient and hot blackbody views using
325 the complex arithmetic technique proposed by Revercomb et al. (1988). However, careful analysis
326 has shown that there can still exist a slight positive bias to the observed sky radiance; this is most
327 easily seen in extremely dry clear sky scenes (Delamere et al., 2010; Turner, 2003). Initially, the
328 source of this bias was assumed to be something in the foreoptics (e.g., some scattered light), and
329 Delamere et al. (2010) assumed that there was a small fraction (order 0.1%) of ambient radiation
330 scattered into the sky observations. However, extensive analysis across multiple AERI systems,
331 including a detailed examination during a particular low radiance condition, ruled out all
332 contributions from the foreoptics (e.g., scattered radiation, polarization) and the Revercomb
333 calibration method rules out phase issues. A new hypothesis was formulated suggesting that
334 emission from the aft optics is not accounted for in the calibration. The functional form of an aft
335 optics correction would be the same as used in Delamere et al. (2010), with the contribution from
336 the “offending” temperature being that of the aft optics. For this study, the observations did not
337 definitively support either an issue with the foreoptics or the aft optics, so no bias correction was
338 applied.

339
340 Fig. 8 shows average AERI radiances from observations used in this study for different PWV
341 ranges.

342
343 **3.2 Model Calculations**

344 Radiance calculations by LBLRTM_v12.15.1 are used in our radiative closure analysis, which
345 focuses on the 780-1280 cm^{-1} region. Absorption line parameters used in these calculations utilize
346 the line file version AER_v3.8.1 and continuum absorption is specified by MT_CKD_4.1.1 (for
347 our baseline calculations). (These models and databases are available at [https://github.com/AER-](https://github.com/AER-RC)
348 [RC](https://github.com/AER-RC), the GitHub repository of the AER Radiation and Climate Group.) We also perform LBLRTM
349 calculations for which the water vapor continuum is changed to MT_CKD_4.1.1+BL. All
350 calculations used in this study include all relevant absorption due to water vapor, carbon dioxide

351



352 **Fig. 8.** Average AERI radiances used in this study from MAO (blue curve) and for two PWV bins at SGP
 353 (red and green curves). A “radiance unit” (RU) is $1 \text{ mW} / (\text{m}^2 \text{ sr cm}^{-1})$.

354
 355 (including first-order line coupling), ozone, nitrous oxide, methane (first-order line coupling),
 356 ammonia, CCl₄, CFC-11, CFC-12, HNO₃, HCFC-22, and PAN.

357
 358 The MT_CKD water vapor continuum model (Mlawer et al., 2023; Mlawer et al., 2012) provides
 359 water vapor self and foreign continuum coefficients ($\text{cm}^2/\text{molecule}/\text{cm}^{-1}$) every 10 cm^{-1} from 0-
 360 20,000 cm^{-1} . To obtain continuum coefficients in between the stored values, a cubic interpolation
 361 using the four closest stored values is performed. Absorption coefficients C_x ($\text{cm}^2/\text{molecule}$) can
 362 be obtained by multiplying the continuum coefficients \tilde{C}_x by the radiation term R :

363
 364
$$C(\nu, T, \rho_x) = \tilde{C}_x(\nu, T, \rho_x) R(\nu, T) \quad (1)$$

365
 366 where ν is the wavenumber, T is the temperature, the subscript ‘x’ denotes either ‘self’ or ‘foreign’,
 367 and the radiation term R is given by

368
$$R(\nu, T) = \nu \tanh\left(\frac{h\nu}{2kT}\right), \quad (2)$$

369

370 where h is Planck's constant, c is the speed of light, and k is Boltzmann's constant. The dependence
 371 on density implied by the notation for \tilde{C}_x is given by

$$372 \quad \tilde{C}_x(\nu, T, \rho_x) = \tilde{C}_x(\nu, T, \rho_{x,ref}) \left(\frac{\rho_x}{\rho_{x,ref}} \right) \quad (3)$$

373 where ρ is the density of the gaseous molecules interacting with water vapor in the respective
 374 process (i.e. water vapor for the self continuum; all gaseous molecules except for water vapor for
 375 the foreign continuum) and the reference density at which coefficients are stored corresponds to a
 376 pressure of 1013 mbar and a temperature of 296K. The optical depth of the self or foreign
 377 continuum is given by the product of the absorption coefficient C_x and the water vapor column
 378 amount W (molecules/cm²):

$$379 \quad \tau_x(\nu, T, \rho_x) = W(H_2O) C(\nu, T, \rho_x). \quad (4)$$

380
 381 The temperature dependence of the self continuum coefficients in the MT_CKD model is given
 382 by

$$384 \quad \tilde{C}_s(\nu, T) = \tilde{C}_s(\nu, 296K) (296/T)^{n(\nu)} \quad (5)$$

385
 386 where n is a wavenumber-dependent dimensionless parameter and the density dependence of the
 387 coefficients has been suppressed for clarity. The foreign continuum coefficients are assumed to
 388 not be dependent on temperature.

389
 390 More details about this formulation can be found in Mlawer et al. (2023).

391 392 **3.3. Input to the Model**

393 Multiple observations are used to create the profiles used as input to the model calculations. The
 394 foundation for the temperature and water vapor profiles are observations by radiosondes (hereafter
 395 sondes), which were usually launched four times daily during our study period at SGP and twice
 396 a day at MAO. However, sonde measurements are not directly used as input to the radiative transfer
 397 calculations in our analysis. The sonde launch location at SGP is ~250 m from where the AERI is
 398 deployed so its measured temperatures and humidity values in the lowest several hundred meters
 399 cannot provide the needed accuracy for our closure study, and sonde humidity measurements have

400 well known accuracy issues (Turner et al., 2016). For our study, we use the TROPoe (Turner &
401 Löhnert, 2014) physical retrieval algorithm to retrieve profiles of temperature and humidity that
402 provide closure with the sonde profiles, the AERI radiance observations between 538 and 722 cm^{-1}
403 ¹ (i.e., regions of the spectrum wherein the water vapor line shape and continuum absorption have
404 undergone validation (Delamere et al., 2010; Mlawer et al., 2019), and the brightness temperatures
405 at 23.8 and 31.4 GHz from a microwave radiometer (MWR; Cadeddu et al., 2013). For this study,
406 the TROPoe retrieval utilizes the latest version of the MT_CKD continuum (Mlawer et al., 2023)
407 and the AER line file, ensuring that its water vapor spectroscopy from 538-722 cm^{-1} includes recent
408 upgrades.

409

410 The TROPoe algorithm is a 1-dimensional variational retrieval approach using the optimal
411 estimation framework. It has been extensively modified to include a wide number of measurements
412 (with their uncertainties) from different instruments in the observation vector (Turner & Blumberg,
413 2019; Turner & Löhnert, 2021). A prior dataset is used to constrain the retrieval; for the SGP,
414 sonde launches from over 10 years were used to create seasonal priors, whereas all the sondes
415 launched during the Go-Amazon field campaign were used to create the single yearly prior for the
416 MAO site. Ultimately, the retrieval finds the solution (i.e., the retrieved thermodynamic profiles)
417 that provides the best fit with all the observations (i.e., sonde, AERI radiances, and MWR
418 brightness temperatures) and the prior (within their uncertainties). The TROPoe retrieval is run at
419 the sonde launch time.

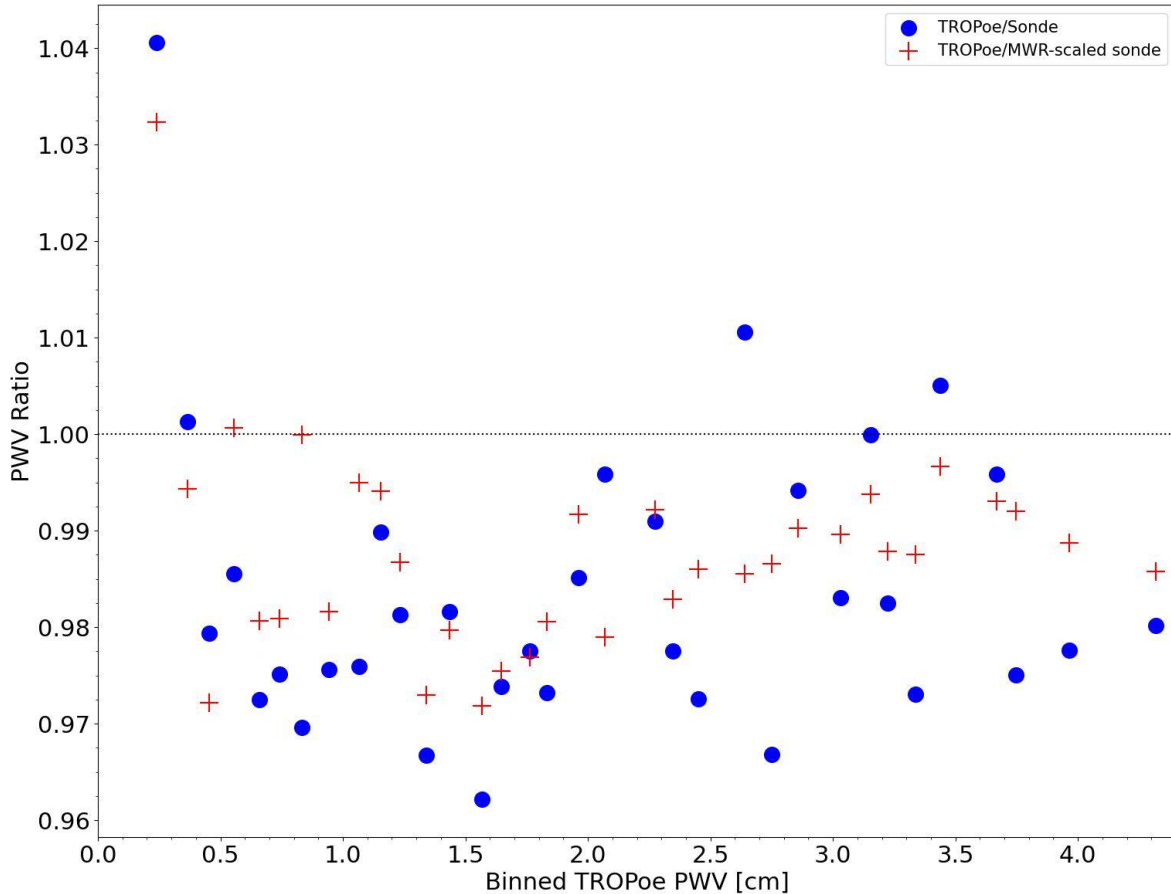
420

421 The TROPoe profiles only extend to 17 km, as that is the maximum height of the prior dataset
422 used to constrain the retrieval. Above 17 km, water vapor values are taken from reference
423 atmospheric profiles (U.S. standard for SGP, tropical for MAO) (Anderson et al., 1986). For
424 temperature, Modern-Era Retrospective analysis for Research and Applications, Version 2
425 (MERRA-2; Randles et al., 2017) profiles are used above 17 km.

426

427 Below, in the uncertainty analysis (section 4.5) of the water vapor continuum absorption
428 parameters derived in this study, an alternative data set of temperature and water vapor profiles is
429 also considered. This specification directly uses the sonde-measured temperature and water vapor
430 profiles in which the sonde water vapor measurements are scaled such that agreement is attained

431 between the 23.8 GHz measurement of the collocated MWR and a corresponding radiative transfer
 432 calculation (Turner et al., 2016). This method to specify the thermodynamic profile has been
 433 previously used in similar radiative closure studies (e.g. Turner et al., 2004; Mlawer and Turner,
 434 2016). For the SGP cases used in this study, the ratios of the PWV values of the TROPoe-derived
 435 and sonde profiles are shown in Fig. 9. Also shown in this figure are the ratios of the PWV values
 436 of the TROPoe-derived and MWR-scaled sonde profiles.



437 **Fig. 9.** Ratios of PWV derived from TROPoe retrieval to the sonde-measured (blue circles) and MWR-
 438 scaled (red plus symbols) PWVs at SGP.
 439

440 The profiles of trace gas abundances that are used in the radiative transfer calculations are obtained
 441 from multiple sources. MERRA-2 profiles corresponding to the SGP and MAO locations are used
 442 to specify ozone. For CO₂, N₂O, CH₄, HCOOH, HNO₃, and PAN, monthly climatologies are used
 443 that were originally developed for the NASA Aura satellite project and updated over time by the
 444 Tropospheric Emission Spectrometer (TES; Worden et al., 2007) and Tropospheric Ozone and its
 445 Precursors from Earth System Sounding (TROPESS; Fu et al., 2013) teams. For four other

446 molecules (CCl₄, CFC-11, CFC-12, and HCFC-22), abundance values from the NOAA
447 Halocarbons and other Atmospheric Trace Species (HATS) program
448 (<https://gml.noaa.gov/hats/flask/flasks.html>) are used. All other molecular profiles are specified
449 using the reference values stored in LBLRTM (U.S. standard atmosphere for SGP, tropical
450 atmosphere for MAO).

451

452 **4. Results of Measurement-Calculation Comparisons**

453 *4.1. Case and channel selection*

454 More than 3000 sondes were launched at SGP during our study period. For each sonde, AERI
455 measurements within a 35-minute window associated with each sonde launch (t-5 to t+30 minutes)
456 are averaged. Given the large number of sondes and the many AERI channels in the targeted
457 spectral region (780-1280 cm⁻¹), we can be selective with respect to the AERI radiance
458 measurements we use in the study to minimize the possibility that our analysis is affected by
459 clouds, insensitivity to water vapor continuum absorption, and trace gas uncertainty.

460

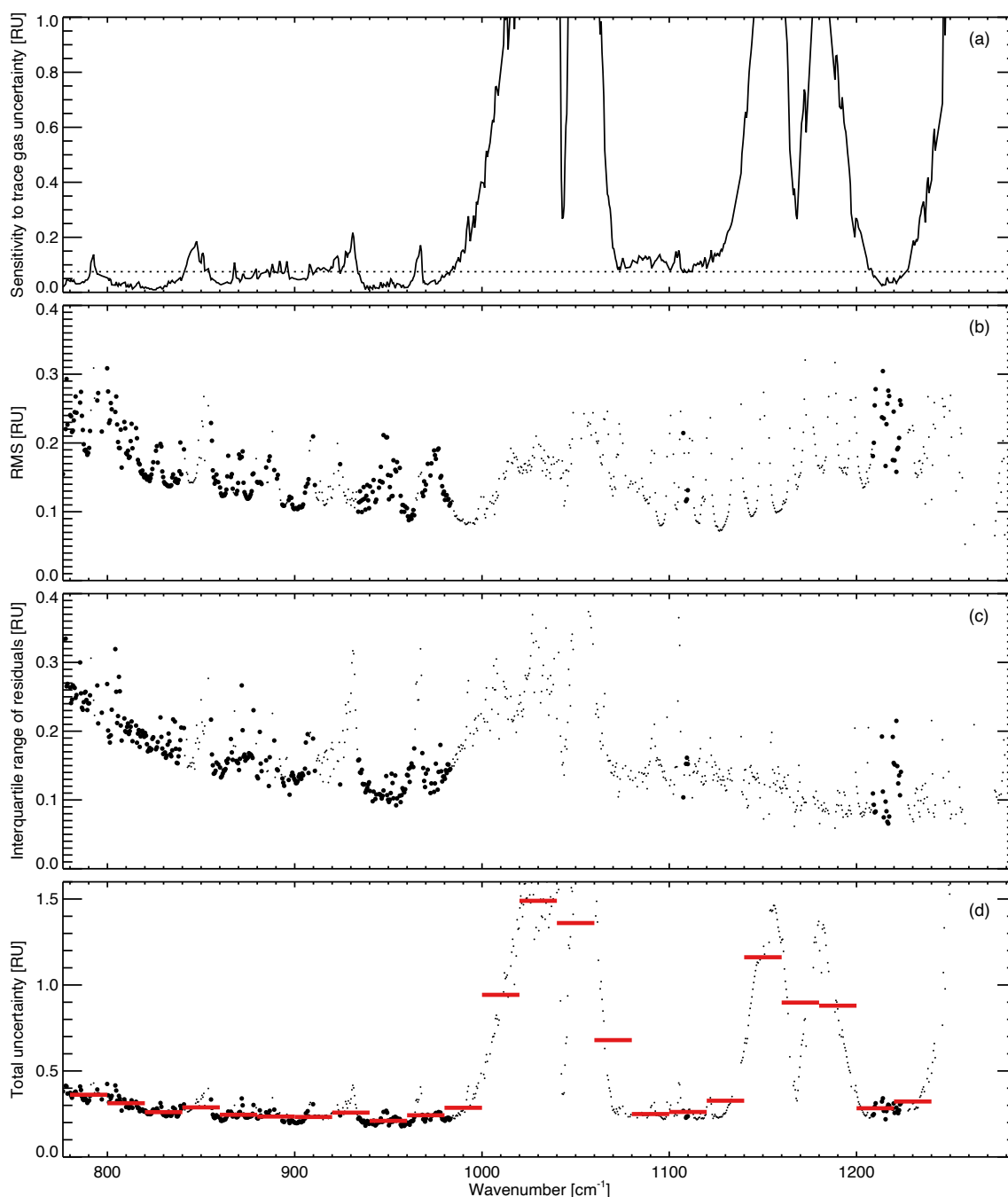
461 To avoid cloud contamination, we remove from our analysis all cases where a cloud might be
462 contributing to the downwelling infrared radiance using two tests: the cloud liquid water path
463 retrieved by TROPoe is less than 2 g/m², and the magnitude of the standard deviation of the 900
464 cm⁻¹ radiance observation over the 35-minute window is less than 0.3 RU. This initial screening
465 removes AERI spectra that fail either of these tests for the presence of clouds, resulting in 453
466 AERI spectra being identified as clear-sky observations.

467

468 Our analysis of the water vapor continuum focuses on AERI channel measurements that are
469 sensitive to the strength of water vapor continuum absorption. These spectral elements are
470 identified by evaluating the sensitivities of all AERI channels to a change in continuum strength.
471 We first compute the change in spectral radiances for all clear AERI cases due to a small
472 perturbation in the self continuum, then bin these sensitivity values in 10 cm⁻¹ spectral bins and
473 five PWV ranges. For each spectral bin and PWV range, we classify each channel in all AERI
474 cases as either “sensitive” or “insensitive” by computing a threshold between the two classes based
475 on minimizing the combined variance in both classes (Otsu, 1979). AERI channels that are
476 classified as “sensitive” for at least 50% of the cases in at least three of the five PWV ranges are

477 used in the SGP analysis, and the other channels are not considered further in our retrieval of water
478 vapor continuum coefficients.

479
480 Given the very low optical depths associated with the foreign continuum (Fig. 3), a small error in
481 the specification of trace gas abundances can impact the determination of foreign continuum
482 coefficients from the AERI measurements. Any such error in the foreign continuum may then
483 cascade through the analysis, impacting the accuracy of the derived self continuum. To identify
484 AERI channels that may be non-trivially impacted by inaccurate specification of trace gas
485 abundances, the uncertainty for each abundance value is required. In this analysis, we use a
486 conservative estimate of ~ 2 ppm for CO_2 , while the uncertainty in the total column amount of N_2O
487 is estimated as 1% and CH_4 as 0.02 ppmv. For HNO_3 and PAN, the uncertainty was calculated as
488 the standard deviation of the monthly values for this location in the climatologies. For NH_3 and
489 HCOOH , we use estimated uncertainties of 50%. For ozone, following Wargan et al. (2017) the
490 stratospheric and tropospheric uncertainties are estimated as 8% and 21%, respectively. For CCl_4 ,
491 CFC-11, CFC-12, and HCFC-22, the uncertainty is set to be consistent with the variance of the
492 respective source value in the HATS database. Using the uncertainty values for all trace gases, a
493 sensitivity study is performed corresponding to an AERI observation associated with a moderate
494 PWV value (2.15 cm) and spectral differences are computed between a baseline calculation in
495 which the trace gases are at their standard abundances and a perturbed calculation in which these
496 abundances are increased by their respective uncertainties. The results from these calculations are
497 shown in Fig. 10a. For a chosen uncertainty threshold value of 0.075 RU, we consider water vapor
498 continuum coefficients derived at spectral points for which the sensitivity to trace gas abundances
499 exceeds this threshold to be less reliable, while those AERI channels below this threshold and thus
500 showing less sensitivity to trace gas uncertainty are considered more reliable. Certain figures in
501 this paper (Figs. 10, 12, 13, and 14) distinguish between these two categories of AERI channels
502 through the use of large circles (greater confidence) and small circles (lesser confidence). (The
503 uncertainty threshold is significantly exceeded throughout the ozone band from $980\text{-}1080\text{ cm}^{-1}$ and
504 radiative closure results in this spectral region are not presented in this study to avoid confusion.)
505



506 **Fig. 10.** For AERI channels from 780-1280 cm^{-1} : (a) Difference in calculated radiances due to the changes
 507 to abundances of trace gases described in the text. The analysis in this study at spectral locations for which
 508 this change is less than the horizontal dotted line shown are viewed with greater confidence; (b) RMS
 509 differences between radiances calculated with profiles utilized in this study and reasonable alternate profiles
 510 (as described in text); (c) Interquartile range of measurement-calculation differences for all PWV bins; (d)
 511 Total spectral uncertainty of measurement-calculation residuals (black circles) and RMS of uncertainties in
 512 20 cm^{-1} regions (red horizontal lines).
 513

514

515 **4.2. Initial analysis**

516 For each selected AERI channel, the residuals between the AERI radiance measurements and
517 corresponding LBLRTM calculations are grouped into 0.1 cm PWV bins. Since the values of some
518 residuals in each bin can differ greatly from the median residual in that bin, we eliminate the impact
519 of possible outliers only considering the results in a PWV bin for cases that have a residual between
520 the 25th and 75th quartiles. The mean of this “inner half” of cases is computed for all PWV bins
521 (for each set of LBLRTM calculations considered in this study).

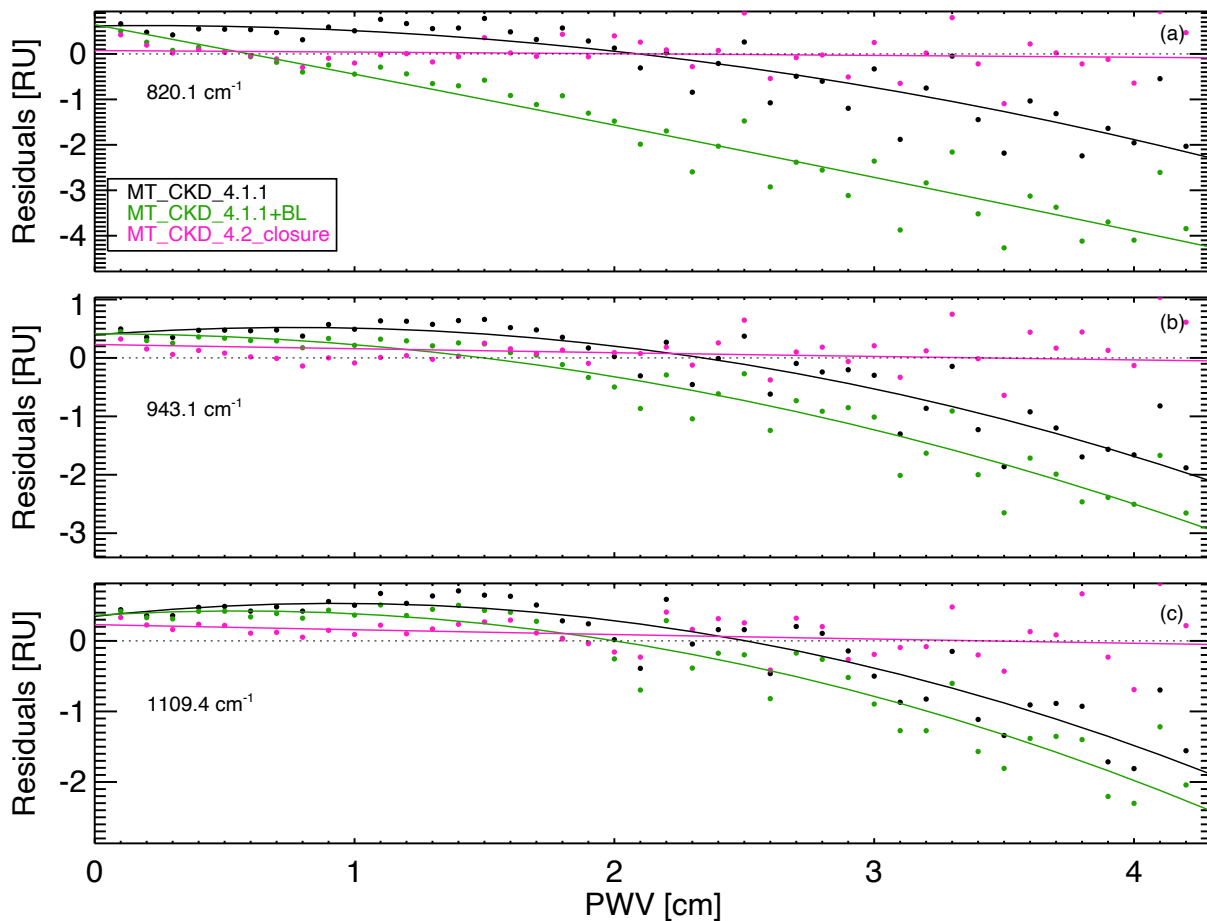
522

523 The behavior of these binned mean residuals as a function of PWV is shown in Fig. 11 for three
524 AERI channels. Results are shown for LBLRTM calculations that use MT_CKD_4.1.1 (black) and
525 MT_CKD_4.1.1+BL (green; description in section 2). The dependence of the residuals on PWV,
526 fit with a quadratic function for each channel, indicates that the measurement data set is not
527 consistent with the LBLRTM calculations for either of these specifications of self and foreign
528 water vapor continuum absorption. Furthermore, the behavior of the residuals as a function of
529 optical depth suggests that more atmospheric opacity is needed in the calculation for low PWV
530 amount, while the opacity is overestimated for higher PWV values. Other channels in the infrared
531 window show similar results.

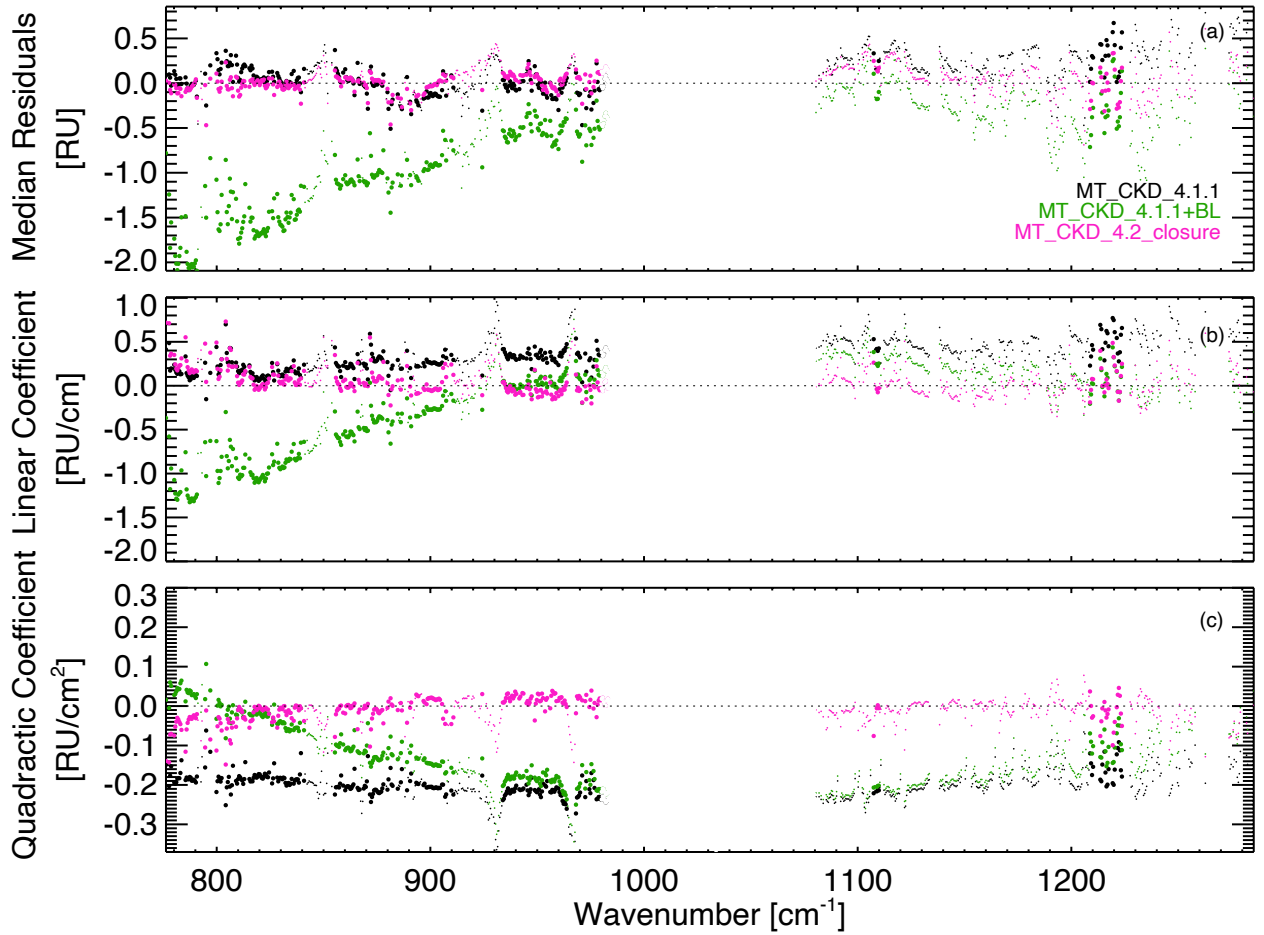
532

533 The medians (over PWV bins) of the inner half mean residuals for calculation using
534 MT_CKD_4.1.1 (black) and MT_CKD_4.1.1+BL (green) are shown in the top panel of Fig. 12
535 for each AERI channel analyzed. Although MT_CKD_4.1.1 appears to provide reasonable results,
536 the results in this panel are misleading. As for the three channels shown in Fig. 11, a quadratic
537 curve is fit to the values of binned mean residuals vs. PWV for all AERI channels. The linear and
538 quadratic coefficients of the fit for each channel are shown in the bottom two panels, respectively,
539 of Fig. 12. Reasonable overall agreement between the measured and calculated radiances would
540 result in residuals that would have little dependence on PWV -- the values in each of the bottom
541 two panels of Fig. 12 would be more-or-less zero (i.e. follow the panel’s x-axis). This is not the
542 case for either version of LBLRTM available prior to this study.

543



544 **Fig 11.** Residuals between AERI measurements at SGP and corresponding LBLRTM calculations as a
 545 function of PWV for three AERI channels in the infrared window. The black symbols are for LBLRTM
 546 calculations that use MT_CKD_4.1.1, the green symbols correspond to the use of MT_CKD_4.1.1+BL,
 547 and the pink symbols result from using the continuum derived in this study, MT_CKD_4.2_closure.
 548 Quadratic fits to these residuals are shown as curves in corresponding colors. Cases are binned by PWV
 549 and analyzed as described in the text.
 550



551 **Fig. 12.** Comparison between AERI measurements at SGP and corresponding LBLRTM calculations for
 552 the spectral region 780-1280 cm^{-1} : (upper) Median of the PWV-binned residuals. The residual for each
 553 spectral point in a PWV bin is computed as the mean of the “inner half” of all residuals in that bin, as
 554 described in the text. The black symbols are for LBLRTM calculations that use MT_CKD_4.1.1, the green
 555 symbols correspond to MT_CKD_4.1.1+BL, and the pink symbols result from using the continuum derived
 556 in this study, MT_CKD_4.2_closure; (middle) Linear coefficient of the quadratic fit to the residuals as a
 557 function of PWV; (bottom) Quadratic coefficient of the quadratic fit to the residuals as a function of PWV.
 558 The distinction between large and small circles in all panels is explained in the text.
 559

560 Since the foreign continuum depends linearly and the self continuum quadratically on the water
 561 vapor amount, there is some validity in associating the behavior of the linear fit coefficient shown
 562 in Fig. 12b with an inaccurate specification of the foreign continuum and the behavior of the
 563 quadratic coefficient (Fig. 12c) with the self continuum. However, due to the dependence of each
 564 on pressure, and hence on the water vapor profile and not simply on PWV, and the dependence of
 565 the self continuum coefficients on temperature, such an association is not exact. A modification in
 566 the specification of either continuum source will lead to changes in both the linear and quadratic

567 fit coefficients, so improvements to the results shown in Fig. 12 can follow only from a
568 simultaneous analysis of the foreign and self continua.

569

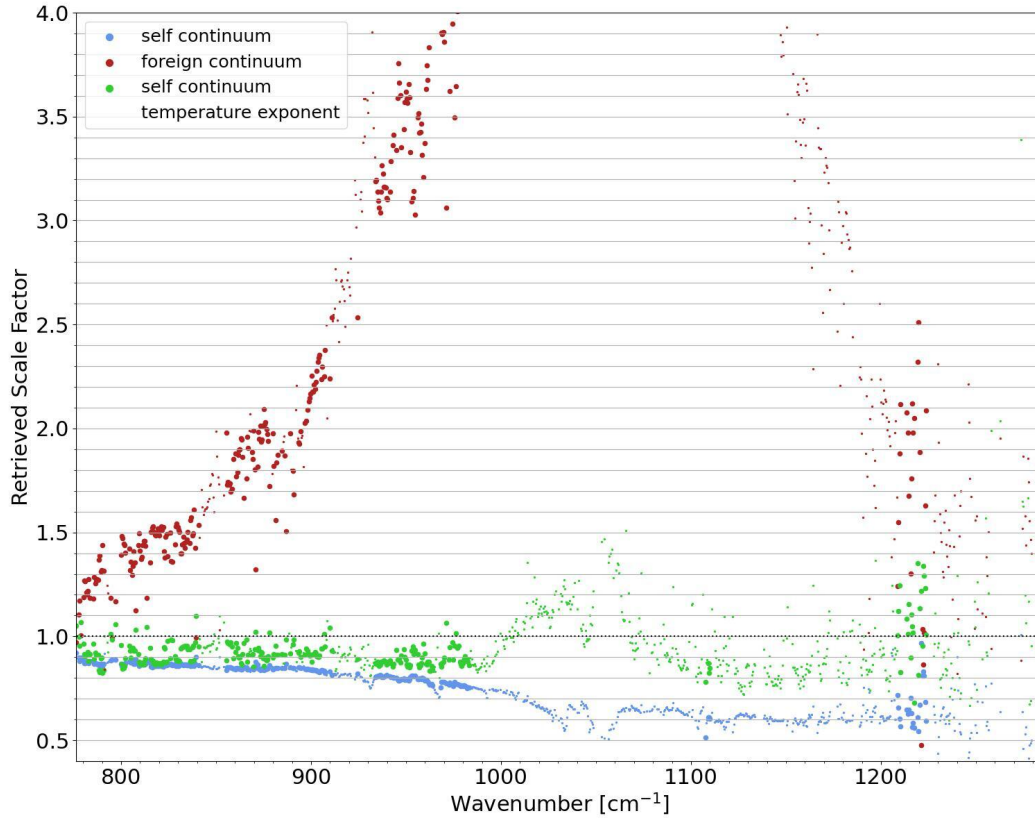
570 *4.3 Retrieval of Self and Foreign Continua*

571 Our SGP AERI dataset, with its large number of cases and wide range of PWV values, is ideal for
572 retrieving self and foreign continuum coefficients in the infrared window. The wide range of
573 temperatures that characterize the water vapor profiles associated with these AERI observations
574 also may possibly allow the derivation of coefficients that characterize the temperature dependence
575 of the self continuum. Continuum properties determined in the analysis of SGP cases are then
576 validated using AERI measurements from MAO. Due to the high PWV amounts for the MAO
577 cases, this validation is especially informative with respect to the properties of the crucial self
578 continuum.

579

580 The retrieval of water vapor continuum properties in the infrared window begins with baseline
581 LBLRTM calculations of downwelling surface radiances for all the cases in the SGP AERI data
582 set. These initial LBLRTM calculations utilize MT_CKD_4.1.1+BL (i.e. corresponding to the
583 green results in Fig. 12), although the retrieval results are fairly insensitive to this choice. Using
584 the measurement-calculation residuals, for each AERI channel between 780-1280 cm^{-1} a least-
585 squares retrieval is performed of three independent variables -- two linear scale factors, one each
586 for the self and foreign continuum coefficients used in the LBLRTM calculations, and a scale
587 factor for the exponent of the self continuum temperature dependence. The sensitivities of the
588 residuals to changes in the retrieved continuum properties (i.e. the Jacobian) used in the retrieval
589 are obtained from additional sets of LBLRTM calculations in which each of these three properties
590 is perturbed by a small amount. In the methodology, we apply the PWV binning discussed above.
591 That is, at each spectral point a single residual and corresponding sensitivities are computed for
592 each PWV bin by averaging the “inner half” of the residuals for all the cases in that bin. With this,
593 each least-square retrieval operates on 43 (the number of PWV bins) measurement-calculation
594 residuals. A three-variable retrieval is run to obtain scale factors for the self continuum, foreign
595 continuum, and temperature exponent of the self continuum. Fig. 13 shows the results of this
596 retrieval.

597



598 **Fig. 13.** Scale factor values (relative to MT_CKD_4.1.1+BL) obtained from the initial retrieval step
 599 described in the text for the self continuum (blue), foreign continuum (red), and self continuum
 600 temperature exponent (green). The distinction between large and small circles is the same as in Fig 12.
 601

602 Using these results, an interim revised version of the MT_CKD water vapor continuum is created
 603 by smoothing the retrieved spectral coefficients, interpolating through the ozone band region, and
 604 blending the retrieved values into the continuum values in neighboring regions. Then the entire
 605 retrieval process is repeated, including new sensitivity calculations using the interim MT_CKD
 606 version. This process is iterated several times until the properties until no further smoothly varying
 607 change in the continuum parameters could further improve the results (i.e. the median residuals
 608 and the linear and quadratic coefficients of the fit of the residuals with respect to PWV).
 609

610 The median values of the measurement-calculation residuals using the final retrieved continuum
 611 coefficients and temperature dependence (MT_CKD_4.2_closure) are shown in pink in Fig. 12a.
 612 As before, a quadratic function is fit to these residuals at each spectral point and the fit coefficients
 613 are shown in Fig. 12b and c. Fig. 11 shows in pink the quadratic fit for MT_CKD_4.2_closure for
 614 the same example AERI channels shown in this figure for prior versions of MT_CKD. These

615 figures indicate that the properties of the residuals between the SGP AERI measurements and
616 LBLRTM residuals are greatly improved when MT_CKD_4.2_closure is used in the calculations
617 compared to previous continuum versions. This improvement has resulted from increasing the
618 atmospheric opacity for low PWV cases (roughly $PWV < 2$ cm) while decreasing it for higher
619 PWVs.

620

621 ***4.4 Validation using AERI observations from MAO***

622 As validation, LBLRTM calculations using several versions of MT_CKD are performed for the
623 MAO AERI cases. The median residuals corresponding to these calculations are shown in Fig. 14.
624 As for the SGP analysis above, these medians are computed from the inner half mean residuals of
625 each PWV bin. (Each MAO PWV bin has a width of 0.2 cm.) As for SGP, no bias correction is
626 applied to the MAO AERI measurements. (For the warm and moist conditions of MAO, any such
627 correction would have only a small impact.) Due to the limited range of PWV values in the MAO
628 dataset, quadratic functions are not fit to the residuals. It is clear from Fig. 14 that the residuals
629 using MT_CKD_4.2_closure are greatly improved compared to previous continuum versions.

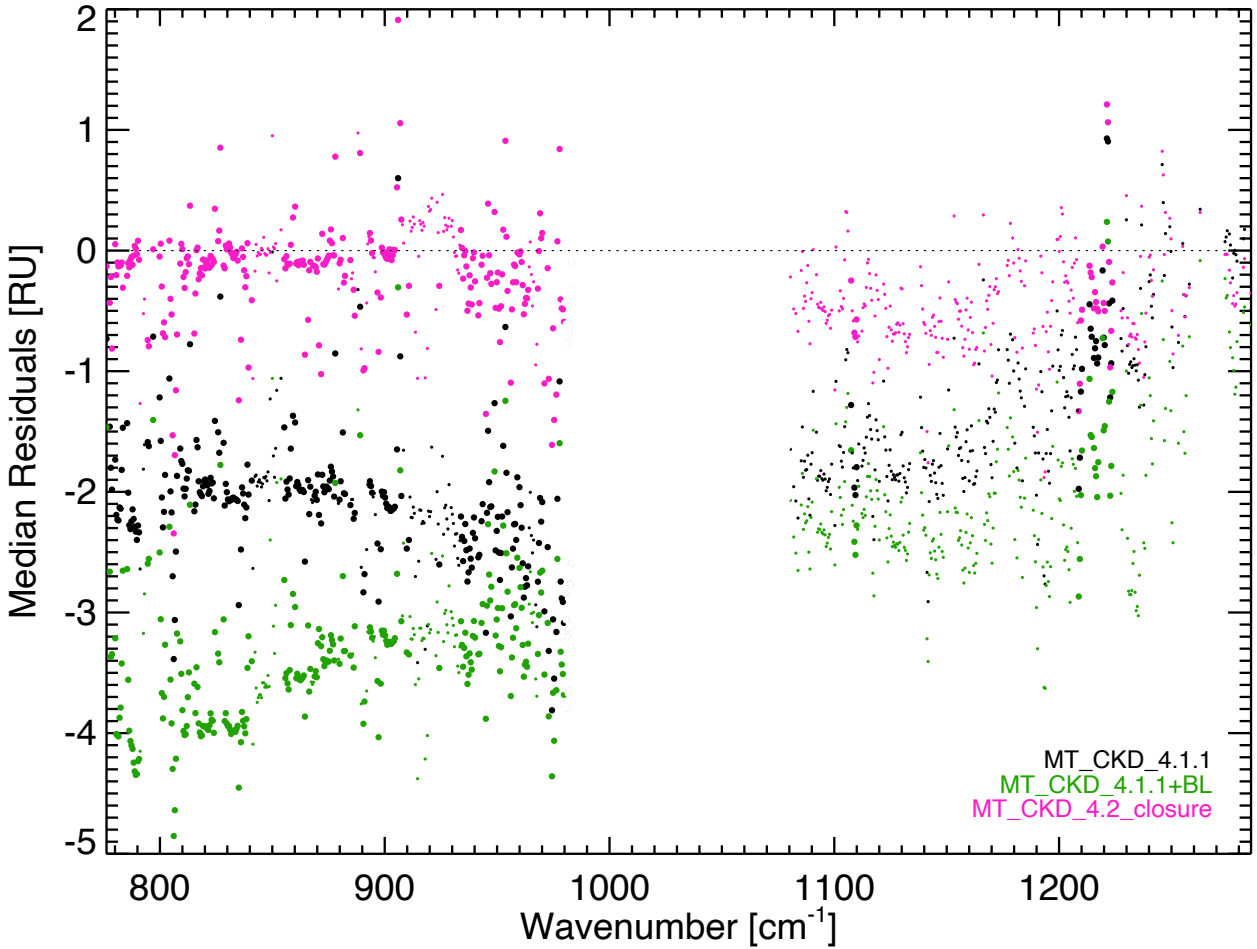
630

631 The self and foreign continuum coefficients retrieved from the SGP AERI measurements in this
632 study are shown (MT_CKD_4.2_closure) in purple in Figs. 4d and pink in Fig. 6, respectively.
633 The retrieved temperature exponents of the self continuum are shown in Fig. 5 (purple). Detailed
634 discussion of these results is provided in section 5.

635

636 ***4.5 An adjustment to the retrieved foreign continuum***

637 The continuum coefficient retrieval described above did not include the spectral region from 990-
638 1070 cm^{-1} , which has significant ozone absorption. In Fig. 6, a reasonable spectral continuation of
639 the AERI-derived coefficients across this region is shown with a thin pink curve segment. The
640 overall flatness of the foreign continuum coefficients in the $900\text{-}1150\text{ cm}^{-1}$ region does not agree
641 with the corresponding relative behavior of the coefficients derived by Baranov and Lafferty
642 (2012) or that of MT_CKD_4.1.1, both of which have much smaller continuum coefficients in the
643 middle of this region ($\sim 1070\text{ cm}^{-1}$) than at its endpoints. For MT_CKD_4.1.1, this deep well is a



644 **Fig. 14.** Median of the PWV-binned residuals between AERI measurements at MAO and corresponding
 645 LBLRTM calculations for the spectral region 780-1280 cm⁻¹. The residual for each spectral point in a PWV
 646 bin is computed as the mean of the “inner half” of all residuals in that bin, as described in the text. Residuals
 647 are shown for MT_CKD_4.1.1 (black), MT_CKD_4.1.1+BL (green), and MT_CKD_4.2_closure (pink).
 648 The distinction between large and small circles is the same as in Fig 12.
 649

650 natural consequence of the assumption that the continuum in this region is due to the sum of
 651 transitions centered hundreds of wavenumbers away from this window region (e.g. at 100 cm⁻¹),
 652 with the continuum absorption from each transition decaying rapidly with increasing wavenumber
 653 far (e.g. 800-1000 cm⁻¹) from its center. Based on its generally flat behavior from 900-1150 cm⁻¹,
 654 we conclude that the MT_CKD_4.2_closure (pink) curve in Figure 6 likely does not represent the
 655 actual behavior of the foreign continuum in this region.

656

657 The optical depths in this region from the MT_CKD_4.2_closure foreign continuum are small.
 658 Fig. 15a shows the derived foreign continuum optical depths at 980 cm⁻¹ for all the cases in the

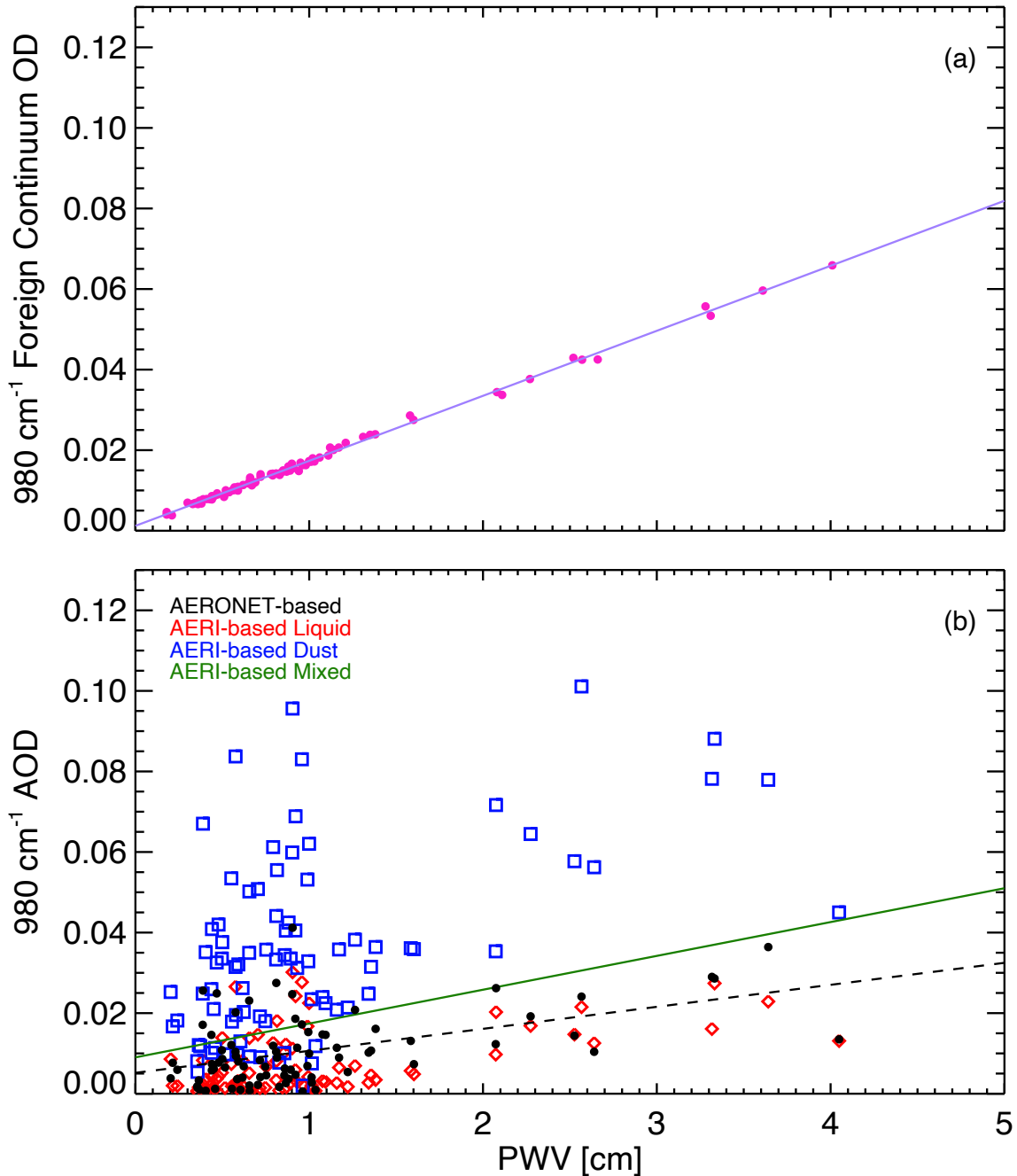
659 SGP data set. For a PWV of 2 cm, this optical depth is ~ 0.03 . At SGP, if there existed an
660 atmospheric constituent with a small optical depth that scaled somewhat linearly with PWV, then
661 the impact in our analysis of such a constituent would be to inflate the derived foreign continuum
662 optical depth above the actual foreign continuum, and this artificial inflation would
663 disproportionately affect the derived foreign continuum most where it is smallest, i.e. the 980-1120
664 cm^{-1} region.

665

666 We now explore the possibility that the presence of aerosol in the skies over SGP can lead to such
667 an overestimation of the foreign continuum in our analysis. We obtain retrievals of aerosol optical
668 depth (AOD) with two markedly different approaches. We analyze periods coincident with the
669 daytime cases in our data set, and assume that the daytime result are representative of the entire
670 data set.

671

672 The first approach is to retrieve aerosol optical depth (AOD) and aerosol refractive index (RI)
673 within one hour of the AERI observations at SGP used in our analysis from the Aerosol Robotic
674 Network (AERONET; Dubovik & King, 2000). We estimate the AOD at $\sim 1000 \text{ cm}^{-1}$ ($10 \mu\text{m}$) from
675 AERONET observations at shortwave infrared (longest wavelength observed is 1640 nm) and
676 visible wavelengths coupled with assumptions about aerosol composition. We assume that the
677 AOD at longer wavelengths is dominated by contributions from an external mixture of coarse-
678 mode aerosols composed of deliquescent aerosol (produced through hygroscopic growth) and
679 mineral dust. The RI of deliquescent aerosol converges with that of water, 1.3 at 1640 nm and 1.2
680 $+0.05i$ at $10 \mu\text{m}$. The RI of dust depends on the composition, which is assumed to be iron-
681 oxide/hematite, a common soil component for the SGP region, having an index of refraction of
682 about 1.6 at 1640 nm and $2+0.02i$ at $10 \mu\text{m}$. We allow the retrieved real part of the RI which spans
683 the range from 1.3 to 1.6 μm to dictate the relative fraction of deliquescent aerosol to dust, and
684 thus infer the effective RI of the external mixture at $10 \mu\text{m}$. Lastly, we use Mie scattering theory
685 to extend the measured AOD from shorter wavelengths out to $\sim 10 \mu\text{m}$. Clearly, the deliquescent
686 components should have a positive dependence on relative humidity and PWV, a fact that is borne
687 out in Fig. 15b. It is also intriguing and comfortingly consistent that the aerosol Angstrom exponent



688 **Fig 15.** As a function of PWV for the daytime SGP AERI cases analyzed in this study: (a) Foreign
 689 continuum optical depths from MT_CKD_4.2_closure; (b) Aerosol optical depths at 980 cm⁻¹ derived from
 690 AERONET measurements assuming a combination of a deliquescent aerosol and mineral dust (black points
 691 with dashed black fitted line), retrievals from AERI observations at 2500-2860 cm⁻¹ assuming a hydrated
 692 sulfate aerosol (modeled as liquid, red diamonds), retrievals from AERI observations at 2500-2860 cm⁻¹
 693 assuming montmorillonite spheres (dust, blue squares), and a 74/26 combination of the liquid and dust
 694 aerosol assumptions, respectively (green linear fit, individual values not shown for figure clarity). Positive
 695 correlation with PWV is seen for all modeled aerosols.

696 which typically varies between +2 to 0 for shorter wavelengths that are observed by the AERONET
697 system, to be moderately negative (-0.65) over the 1000-1100 cm^{-1} spectral range, driven by
698 changes in the refractive indices that vary notably in the longer wavelength range while being
699 virtually constant at shorter wavelengths.

700

701 The AODs values obtained from this analysis are shown as black circles in Fig. 15b. The results
702 in Fig. 15 show the estimated aerosol optical depth at 980 cm^{-1} is approximately half of the derived
703 foreign continuum optical depth. The aerosol optical depths scale reasonably linearly with PWV,
704 a consequence of the hygroscopicity of ambient aerosol whereby aerosols increase in size through
705 uptake of water vapor from the atmosphere, supporting the inference that the presence of aerosols
706 could have impacted our retrieval of foreign continuum coefficients.

707

708 The second approach to retrieve AOD uses the downwelling radiance observations made by the
709 AERI in the 2500-2860 cm^{-1} (3.5-4.0 μm) spectral region. Since at 2500-2860 cm^{-1} the
710 downwelling AERI radiance observation is dominated by scattered solar radiation during the
711 daytime, in this analysis we use only the daytime AERI samples that coincide with the AERONET
712 observations used in the first approach. We apply the physical-iterative Mixed-phase Cloud
713 Retrieval Algorithm (MIXCRA; Turner, 2005) to these AERI observations assuming that the
714 “cloud” was composed of aerosol particles (as was done in Turner 2008). We apply MIXCRA
715 with two distinct assumptions for aerosol type, one modeling the aerosol as liquid droplets
716 (representing a hydrated sulfate aerosol, shown as red diamonds in Fig. 15b) and the other
717 assuming montmorillonite spheres (i.e. dust, blue squares in Fig. 15b). The Interagency Monitoring
718 of Protected Visual Environments (IMPROVE; Malm et al., 1994) project provides measurements
719 of the mass of sulfate and soil particles that have diameters less than 2.5 μm . Using IMPROVE
720 data from Stilwell, OK (the closest IMPROVE site to ARM SGP during 2016-2018), over our
721 analysis period the mean ratio of the sulfate (liquid) aerosol mass to the sum of the sulfate and soil
722 mass was 0.74. We thus estimate the AOD at 980 cm^{-1} using $0.74 * \text{AOD}_{\text{liquid}} + 0.26 * \text{AOD}_{\text{dust}}$,
723 which yields somewhat higher AOD results (green line in Fig. 15b) as a function of PWV as the
724 first method that was based on AERONET observations.

725

726 These AOD estimates establish that it is plausible that the presence of aerosols has impacted the
727 determination of the MT_CKD_4.2_closure foreign continuum coefficients shown in Fig. 6.
728 However, the assumptions about aerosol properties made in the analyses above are quite
729 speculative and the actual aerosol optical depths in the infrared window may differ significantly
730 from those we derived. The possibility that our continuum coefficient retrieval has been impacted
731 by aerosols leaves us with two choices, each of which has positive aspects and flaws. We could
732 ignore this likely contamination of our derived foreign continuum (MT_CKD_4.2_closure in Fig.
733 6) and its problematic flat spectral behavior, and provide these foreign continuum coefficients in
734 the next release of MT_CKD. This choice, when used in concert with our derived self continuum,
735 would provide radiative closure with the AERI observations used in this study, but likely only
736 because the water vapor continuum in this region inappropriately included some absorption that is
737 actually due to aerosols. The other choice is to use the analysis above to make an estimate of the
738 aerosol contribution to the derived foreign continuum, subtract this initial estimate of this aerosol
739 contamination from MT_CKD_4.2_closure, and then use the MT_CKD line shape methodology
740 (Mlawer et al., 2012) to compute foreign continuum coefficients that are in reasonable agreement
741 with this difference. By construction, this option will have relative spectral behavior in the middle
742 of the window that is similar to the behavior in MT_CKD_4.1.1 (also similar to that measured by
743 Baranov and Lafferty, 2012), but will no longer provide closure with the AERI measurements
744 since calculations using this foreign continuum would be missing optical depth unless a user
745 explicitly included longwave aerosols in their calculation. Another drawback of this approach
746 stems from the realization that any estimate of aerosol absorption in the infrared window would
747 be highly uncertain, which would lead to significant uncertainty in the foreign continuum derived
748 after the aerosol contribution is removed from the MT_CKD_4.2_closure foreign continuum.

749
750 Given this difficult choice, we feel that it is important for the MT_CKD continuum model to
751 provide our best estimate of the actual foreign continuum despite the inherent uncertainty of the
752 approach used to derive it. Therefore, we choose to derive the new foreign continuum for
753 MT_CKD_4.2 by accounting for the estimated contribution of aerosols. Given that the use of
754 MT_CKD_4.2 will not result in radiative closure, we will also provide the MT_CKD_4.2_closure
755 foreign continuum as an alternate foreign continuum choice for users of MT_CKD.

756

757 In Appendix 2, we discuss the approach used to derive a specification of the foreign continuum in
758 the infrared window that is consistent with both a) the closure analysis described in section 3.2
759 interpreted in light of the aerosol absorption analysis above (i.e. in Fig. 15b) and b) the relative
760 spectral behavior of the foreign continuum in this region given by the MT_CKD line shape
761 calculation. This derivation uses the MT_CKD line shape formalism to compute foreign
762 continuum coefficients from 780-1250 cm^{-1} that, once subtracted from the coefficients in
763 MT_CKD_4.2_closure, is roughly consistent with the properties (AOD and Angstrom exponent
764 in the infrared window) of the aerosol absorption derived from the AERONET measurements.

765
766 The foreign continuum coefficients (labeled as MT_CKD_4.2) that result from this aerosol-
767 removing procedure are shown as a purple curve in Fig. 6. Since a similar line shape formalism
768 was used to derive these coefficients as was done for MT_CKD_1.0 (virtually the same as
769 MT_CKD_4.1.1), the MT_CKD_4.2 coefficients also have a minimum near 1100 cm^{-1} . The
770 spectral behavior of the MT_CKD_4.2 coefficients now more closely resemble the Baranov and
771 Lafferty (2012) measurements than the derived coefficients before the assumed impact of aerosols
772 was accounted for. This agreement with an independent measurement of foreign continuum
773 absorption provides a measure of confidence that the aerosol adjustment has some validity.

774
775 Given the modification made to the foreign continuum to obtain MT_CKD_4.2 from
776 MT_CKD_4.2_closure, a few observations are worth pointing out. First, calculations using
777 MT_CKD_4.2 do not provide radiative closure with either the SGP or MAO AERI observations.
778 As shown in Fig. 12, impressive agreement between the observations and calculations is obtained
779 using MT_CKD_4.2_closure, but this closure to some extent is due to the assumed inclusion of
780 the radiative effects of aerosols in that continuum version. Removing that contribution, as has been
781 done to construct MT_CKD_4.2, destroys that radiative closure. Therefore, a comparison between
782 the observations and calculations using MT_CKD_4.2 is not informative and we do not include
783 those results on Fig. 12. Second, the strong agreement shown in Fig. 14 between the MAO AERI
784 measurements and calculations using MT_CKD_4.2_closure occurs even though that continuum
785 version is assumed to include the impact of aerosols at SGP. This is possibly due to reasonably
786 similar aerosol loading at SGP and MAO, both continental sites, and the reduced relative radiative
787 impact of aerosols at MAO compared to SGP given the higher PWV amounts at MAO. Third,

788 some consideration should be given to the results for MT_CKD_4.1.1 and MT_CKD_4.1.1+BL
789 in Fig. 12 in light of the need for the aerosol adjustment detailed above. In both cases, the foreign
790 coefficients in the infrared window in these continuum versions were not derived from field
791 studies, so they could not have been impacted by aerosols in the same way that the
792 MT_CKD_4.2_closure coefficients are assumed to have been. The window self continuum used
793 in these calculations (the same in both versions) was derived by Turner et al. (2004), a radiative
794 closure field study at SGP. It is reasonable that atmosphere opacities in this previous study were
795 affected by a similar aerosol loading as in the current study, and that the self continuum coefficients
796 derived in Turner et al. (2004) implicitly include the radiative effects of the aerosols. Therefore,
797 no further adjustment to these versions is needed to evaluate the behavior of their associated
798 residuals, and it is fair to compare them to those obtained using MT_CKD_4.2_closure, as is done
799 in Fig. 12.

800

801 *4.6 Uncertainty analysis*

802 The determination of the uncertainties in our retrieved values of self continuum coefficients,
803 foreign continuum coefficients, and the temperature dependence of the self continuum in the
804 infrared window is challenging. Consideration must be given to typical uncertainties in radiative
805 closure studies, such as those due to the radiometric instrument and the specification of the
806 atmospheric profile, as well as complexities in this study such as the consideration of the role of
807 aerosols in the derivation of the foreign continuum. We here provide an analysis of key sources of
808 uncertainty in our derived continuum values.

809

810 Our uncertainty analysis is based on the realization that the set of retrieved continuum values (self,
811 foreign, and temperature dependence of self) in MT_CKD_4.2_closure at a spectral point is not
812 the only combination of continuum values that would provide suitable agreement between the
813 observed and calculated radiances. The retrieved values in most small spectral windows (e.g. 10
814 cm^{-1} , the spacing at which MT_CKD stores continuum coefficients) show some variability (see
815 Fig. 13), as do the final residuals shown in Fig. 12. Therefore, we must consider to what extent the
816 retrieved continuum values can be modified while maintaining “good agreement” between the
817 measurements and calculations. How we define “good agreement” must reflect the uncertainties
818 in both the measurements and calculations. Therefore, we must first analyze individual factors that

819 lead to uncertainty in the spectral residuals, and then combine these factors to get a total spectral
820 uncertainty. Then, at each spectral point the total uncertainty in the radiance residuals provides a
821 foundation for evaluating other sets of possible retrieved continuum values – if the residuals
822 generally stay within this uncertainty for all PWV bins for a given set of continuum values, then
823 these alternate values are considered plausible. Using this approach, we can find limits past which
824 good agreement is no longer possible, therefore defining the uncertainty in each continuum
825 parameter.

826
827 Sources of uncertainty in the radiance residuals arise from the uncertainty in a) the specification
828 of trace gas abundances, b) the temperature and water vapor profiles, and c) the AERI radiance
829 measurements. The method used to determine the uncertainty due to the trace gas specification is
830 discussed above and is shown in Fig. 10a. The uncertainty due to temperature and water vapor
831 profiles is evaluated through the use of a reasonable alternate specification of these profiles, given
832 by sonde measurements in which the measured water vapor profile has been scaled to attain
833 agreement with the brightness temperature measured by a collocated microwave radiometer. This
834 approach to specifying the temperature and water vapor profiles in radiative closure studies has
835 often been utilized in past analyses (e.g. Turner et al., 2004; Mlawer and Turner, 2016; Turner et
836 al., 2016). Fig. 10b shows the spectral RMS differences between calculations that use these
837 alternate profiles and those that use the profiles employed in the analysis described above. Finally,
838 the AERI uncertainty is assigned a value of 0.1 RU based on the random error spectra of the
839 instrument, as estimated by the calibration equation used in its processing (Revercomb et al., 1988;
840 Knuteson et al, 2004b).

841
842 In addition to these contributions to the uncertainty in the residuals, it is clear from Fig. 11 that the
843 variability of the final (pink) residuals as a function of PWV adds an additional challenge in
844 determining what constitutes agreement between measurements and calculations for given
845 continuum parameters. To account for this uncertainty, we compute the interquartile differences
846 of the binned residuals for each spectral point, which is shown in Fig. 10c, and include this as an
847 additional term in the uncertainty calculations.

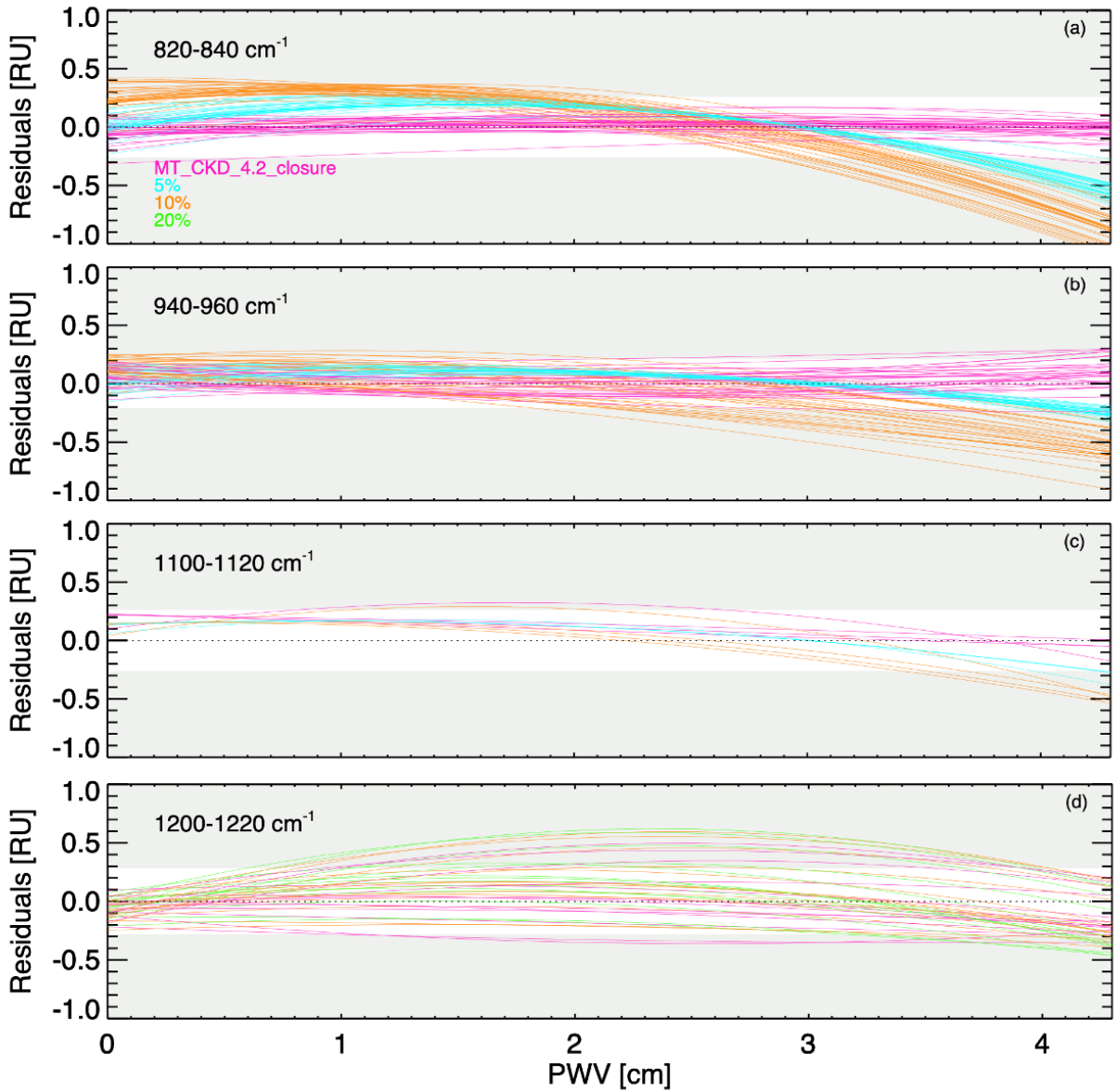
848

849 We assume that these four sources of uncertainty in the residuals are independent and add these
850 values in quadrature at each spectral point to get the spectrum of total uncertainty, shown as black
851 circles in Fig. 10d. Given that the determination of continuum coefficients enforces a degree of
852 spectral smoothness on the coefficients, rather than considering the spectral uncertainty shown in
853 Fig. 10d we group the uncertainty values in 20 cm^{-1} intervals. We take a conservative approach in
854 assigning the final uncertainty value in each interval by using the RMS of the spectral values,
855 which are also shown in Fig. 10d.

856

857 Now we compute alternate sets of continuum coefficients at each spectral point to determine the
858 maximum that each continuum coefficient can be perturbed while keeping the residuals as a
859 function of PWV within the uncertainty in the residuals computed above. We illustrate this
860 procedure for the self continuum. First, all self continuum coefficients in MT_CKD_4.2_closure
861 are increased, in turn, by 5,10, 20, and 30%. For each perturbation, we then follow the procedure
862 detailed in Sec. 4.2 to derive optimal spectral values for the foreign continuum and the temperature
863 dependence of the self continuum. For illustration, quadratic fits to the resulting residuals from
864 these optimal perturbations are shown in Fig. 16 as a function of PWV for all spectral elements in
865 the 20 cm^{-1} bins that contain the wavenumbers in Fig. 11, as well as the $1200\text{-}1220\text{ cm}^{-1}$ bin. (The
866 wavenumber corresponding to each curve shown is not identified since this analysis is being
867 performed collectively for the spectral elements grouped in each interval.) As an example, Fig.
868 16b shows that, for the $940\text{-}960\text{ cm}^{-1}$ region, the coefficients obtained starting with a 5%
869 perturbation to the self continuum result in the residuals staying within the unshaded region, which
870 corresponds to the radiance uncertainty in this region. That is, a 5% perturbation to the self
871 continuum results in measurement-calculation agreement (as defined above). In contrast, the
872 curves corresponding to a 10% perturbation do not remain within the unshaded region, so a 10%
873 change to the self continuum does not lead to agreement. Based on the set of perturbation
874 calculations, for this spectral region we determine that the self continuum uncertainty is 7%. We
875 perform this analysis for all 20 cm^{-1} bins – the resulting self continuum uncertainty values are
876 shown as thin purple error bars on the MT_CKD_4.2 curve in Fig. 4.

877

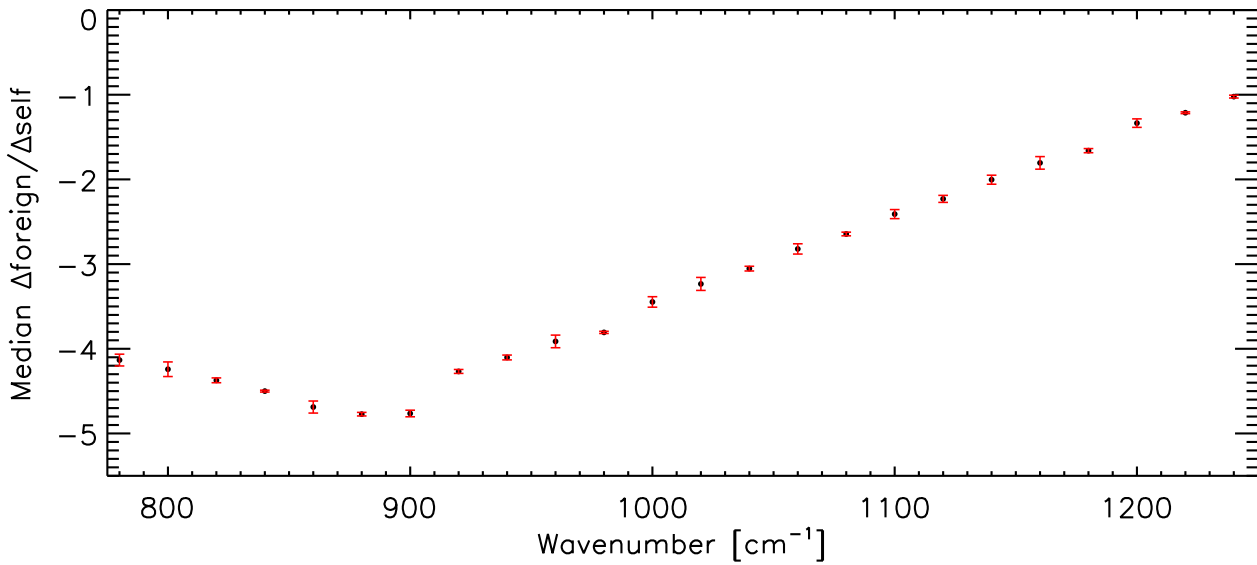


878 **Fig. 16.** For four example 20 cm⁻¹ spectral regions, quadratic fits to the residuals are shown for
 879 MT_CKD_4.2 closure (pink) and variations in which the self continuum has been increased by 5% (cyan),
 880 10% (orange), and 20% (green), with the foreign continuum and self continuum temperature dependence
 881 rederived for each perturbation (as described in text). Curves are shown for the spectral elements
 882 corresponding to the large circles in Fig. 12 and not all colored curves are shown on all panels for clarity.
 883 The regions shaded gray on each panel are outside of the total uncertainty for the respective panels. The set
 884 of colored curves that do not typically stay within the unshaded region shows that the corresponding
 885 perturbation to the self continuum is greater than the self continuum uncertainty in these regions.
 886

887
888 We repeat this procedure starting with a series of foreign continuum perturbations, determining
889 optimal spectral values for the self continuum and the temperature dependence of the self for each
890 perturbation. An analysis similar to the one described above for the self continuum results in the
891 foreign continuum uncertainty values shown in Fig. 6 for MT_CKD_4.2_closure in the 20 cm^{-1}
892 spectral bins. Note that in some spectral regions (primarily the ozone-dominated region from 980-
893 1080 cm^{-1}) this method is not able to determine a reliable uncertainty value for the foreign
894 continuum due to the large uncertainty in the residuals and combined behavior of the self and self
895 temperature dependence in response to the foreign perturbations. In this region, we compute an
896 uncertainty by combining the uncertainty at its boundaries (i.e. 970 and 1090 cm^{-1}) with the
897 difference in continuum values resulting from alternate reasonable ways to span the gap in
898 retrieved (i.e. MT_CKD_4.2_closure) foreign continuum values from 980-1080 cm^{-1} . We discuss
899 below the uncertainty associated with the MT_CKD_4.2 foreign continuum coefficients.

900
901 Finally, we follow this procedure beginning with a series of perturbations to the temperature
902 dependence of the self continuum, determining optimal spectral values for the self and foreign
903 continuum. However, in all spectral bins this method is not able to derive reliable estimates of the
904 uncertainty in the self temperature dependence. Even though the AERI datasets used in our study
905 are not able to effectively constrain the self continuum temperature dependence, below we
906 consider the results of other studies to determine rough estimates of the uncertainty in the
907 MT_CKD_4.2 temperature dependence parameters.

908
909 The continuum parameters derived from the AERI measurements are not independent – for
910 example, an increase in the derived self continuum value at a spectral point would necessitate a
911 lower associated foreign continuum value in order to maintain overall radiative closure at that
912 point. Therefore, for the uncertainty analysis it is informative to understand how these two
913 continuum values co-vary. We therefore perform a retrieval of the foreign continuum value for a
914 small perturbation to the self continuum (with the temperature dependence kept fixed). Fig. 17
915 shows the ratio of the foreign and self continuum changes in these retrievals for the window region.
916 Consideration of the uncertainty in either of these quantities should be done in the context of their
917 combined behavior.



918 **Figure 17.** Ratio of change in derived foreign continuum value to a small perturbation in the self continuum
 919 value.
 920

921 The derivation above of uncertainty values for the MT_CKD_4.2_closure foreign continuum
 922 coefficients does not directly apply to the MT_CKD_4.2 foreign continuum, which was derived
 923 using information other than the AERI measurements at SGP and MAO. The method used to derive
 924 these foreign continuum coefficients was quite speculative, involving a) the
 925 MT_CKD_4.2_closure foreign continuum coefficients, b) ‘best guess’ estimates of the aerosol
 926 optical properties in the infrared window, and c) a calculation using the MT_CKD line shape
 927 formulation constrained to foreign continuum values outside the infrared window and those
 928 inferred in the window from a) and b). The highly conjectural nature of this approach presents
 929 large challenges from using it alone to determine reasonable uncertainty estimates. Instead, we use
 930 all available information (MT_CKD_4.2 closure uncertainties, analysis of the method used to
 931 derive MT_CKD_4.2 foreign continuum, and the laboratory measurements shown in Fig. 6) to
 932 provide users of MT_CKD with a rough estimate of the uncertainty of MT_CKD_4.2 in specifying
 933 water vapor foreign continuum absorption in this region. The upper limit of the uncertainty must
 934 reflect the possibility that the impact of aerosols on the derivation of foreign continuum is
 935 negligible, so the corresponding uncertainty values are determined by the difference between
 936 MT_CKD_4.2 and MT_CKD_4.2_closure (accounting for its own uncertainty). Reassuringly,
 937 even though this uncertainty estimate did not consider the single-frequency measurement of
 938 Cormier et al. (2005), the upper envelope of the MT_CKD_4.2 uncertainty estimates (shown with

939 thin purple vertical bars in Fig. 6) allow the possibility that the foreign continuum is as great as
940 that value. With respect to the lower limit of the MT_CKD_4.2 uncertainty, we explicitly consider
941 the results from the Baranov and Lafferty (2012) study, which is generally lower than the
942 MT_CKD_4.2 coefficients but clearly represent possibly valid values. We compute the uncertainty
943 by adding in quadrature: a) the difference between MT_CKD_4.2 and MT_CKD_4.1.1+BL and
944 b) the uncertainty in the coefficients determined in Baranov and Lafferty (2012). The resulting
945 MT_CKD_4.2 uncertainty estimates are generally consistent with the results we would have
946 attained in our study had we adjusted the MT_CKD_4.2_closure coefficients to account for the
947 impact of aerosol optical depths somewhat greater than we actually assumed (i.e. consistent with
948 the relative aerosol loading of the green line compared to the black line in Fig. 15b). In Fig. 6, we
949 denote MT_CKD_4.2 foreign continuum uncertainty estimates with open-ended vertical lines to
950 contrast the broader perspective used to determine these values with the AERI-based uncertainty
951 estimates used for the MT_CKD_4.2_closure foreign coefficients, which are denoted as (pink)
952 vertical lines with end caps. To conclude, MT_CKD users should be aware of possible
953 considerable uncertainties when utilizing MT_CKD_4.2 foreign continuum coefficients.

954
955 With a similar perspective, we also consider all available information to determine rough
956 uncertainty estimates for the MT_CKD_4.2 temperature dependence exponents, which are not able
957 to be effectively constrained by the AERI measurements used in this study. The upper limit of the
958 uncertainty needs to include the (refit) values from the Burch and Alt (1984) study (accounting for
959 that study's uncertainty) since we view its results with confidence due to the close agreement of
960 its derived self continuum coefficients with those from the current study. (See Fig. 4.) When
961 considering the lower limit of possible values of the temperature dependence exponents, we do not
962 consider the values derived by Baranov et al. (2008) with great confidence since the self continuum
963 coefficients determined in that work do not agree with those derived in the current study. As a
964 result, there is little information to go on to constrain the lower uncertainty limit. We therefore
965 define the uncertainty bars to be equal in the positive and negative directions (adjusted to ignore
966 the bump in the MT_CKD_4.2 exponents centered at 780 cm^{-1}).

967

968 **5. Analysis of MT_CKD_4.2**

969 Fig. 4a shows the final self continuum coefficients (MT_CKD_4.2) derived in this study along
970 with previous versions of the continuum model. With MT_CKD_4.1.1 used as a reference, Fig. 4d
971 shows the relative spectral behavior of MT_CKD_4.2 (and its uncertainty), the most recent
972 laboratory measurements from three groups, previous versions of CKD and MT_CKD based on
973 field studies that have been adjusted (as described in section 2) to account for a larger foreign
974 continuum than utilized in their respective original derivations, and the similarly adjusted results
975 from the field study by Taylor et al. (2003). Although these self continuum specifications do not
976 all agree, it can be argued the evidence clearly suggests that MT_CKD_4.1.1 is too strong across
977 the entire infrared window. For wavenumbers less than 900 cm^{-1} , most of the results shown agree
978 that the self continuum is 8-15% weaker than MT_CKD_4.1.1. Exceptions to this are the study of
979 Baranov et al. (2008) and the adjusted coefficients of CKD_2.1, which is based on the Westwater
980 et al. (1995) study. The adjustment made to CKD_2.1 only accounts for a change in the foreign
981 continuum, but another significant bias in the Westwater et al. (1995) results likely is present. The
982 type of sonde used in the calculations in that study to specify the water vapor fields were
983 subsequently shown to have a dry bias of 4-8% due to contamination of the relative humidity
984 sensor by the packaging (Wang et al. 2002; Turner et al. 2003). Given the squared dependence of
985 the self continuum on water vapor abundance, a rough estimate suggests that the self continuum
986 coefficients derived in that study were likely too high by at least 8%. As a result, the CKD_2.1_adj
987 curve in Fig. 4d likely needs to be shifted downward by that amount to account for this bias. Given
988 that, all results shown in Fig. 4d for $780\text{-}900\text{ cm}^{-1}$ exhibit agreement except for a single outlier
989 result by Baranov et al. (2008). The good agreement of these self continuum specifications persists
990 over the rest of infrared window with the exception of MT_CKD_1.0_adj, which is based on the
991 adjusted results of the Turner et al. (2004) study. It is encouraging that the accurate cavity ring
992 down measurement by Cormier et al. (2005) agrees within the tight uncertainty bound of the
993 current study. In spectral regions in which the uncertainty estimates of the current study are small,
994 the results of the current study are in agreement with all laboratory measurements by Burch and
995 Alt (1984) and most of the adjusted values from the Taylor et al. (2003) field analysis.

996

997 The MT_CKD_4.2 foreign continuum coefficients, which have been adjusted to account for the
998 presence of aerosols at SGP as described above, are shown in Fig. 6. Since its behavior near its
999 minimum results from a similar line shape calculation as MT_CKD_1.0, it is not surprising that

1000 the shapes of these two continuum versions are similar in this region. However, MT_CKD_4.2 is
1001 ~5 times greater than its predecessor in the 960-1150 cm^{-1} region, and 2-4 times greater in the
1002 regions of the infrared window outside this minimum region, i.e. where the continuum is stronger
1003 and the AERI observations provide a greater constraint. In these regions, the MT_CKD_4.2
1004 uncertainty estimates do not include the MT_CKD_1.0 (equivalent to MT_CKD_4.1.1)
1005 coefficients. Despite the quite speculative approach used to adjust the derived foreign continuum
1006 for aerosols, there is some correspondence of these continuum values with the Baranov and
1007 Lafferty (2012) experimental values. By construction, the MT_CKD_4.2 uncertainty estimates
1008 include the Baranov and Lafferty (2012) values.

1009
1010 The self continuum temperature dependence exponents derived in this study are shown in Fig. 5.
1011 As can be seen in Fig. 13, the retrieval of this exponent for 780-980 cm^{-1} shows less variability
1012 than at higher wavenumbers in the region analyzed. Also shown in Fig. 5 are the exponents in
1013 MT_CKD_4.1.1 as well as values derived from the laboratory studies of Baranov et al. (2008),
1014 Cormier et al. (2005), and Burch and Alt (1984). (It is important to note that the exponents shown
1015 on this figure for these studies are for the continuum coefficients as defined in MT_CKD, which
1016 are specified for a reference density and do not include the radiation term.) The Burch and Alt
1017 (1984) study is represented by two sets of alternate temperature exponent values, one based on the
1018 data in the table provided in that work associated with its Fig. 2 and one based on our analysis of
1019 the plotted values in its Fig. 2. It is clear from Fig. 5 that there is no consensus between the
1020 specifications of the self continuum temperature exponents that are displayed. The MT_CKD_4.2
1021 values are in excellent agreement at the single location analyzed in Cormier et al. (2005) and are
1022 closer than MT_CKD_4.1.1 to the Baranov et al. (2008) values in the region where the AERI
1023 analysis is most definitive. Above 980 cm^{-1} , the MT_CKD_4.2 exponents diverge from the
1024 Baranov et al. (2008) values, but there is some suggestion in Fig. 13 that a justifiable choice could
1025 have been made to decrease the MT_CKD_4.2 exponents further, thereby bringing them in closer
1026 agreement to Baranov et al. (2008). Our inability to determine uncertainty values for the exponents
1027 based on the AERI analysis alone reflects that a wide range of exponent values are able (after
1028 adjustments to the self and foreign coefficients) to provide radiative closure with the observations
1029 within the uncertainty in the residuals. Therefore, the exponent values shown in Fig. 5 should be

1030 considered numerical values that optimize the radiative closure results rather than an attempt at a
1031 definitive determination of the spectral behavior of a physical quantity.

1032

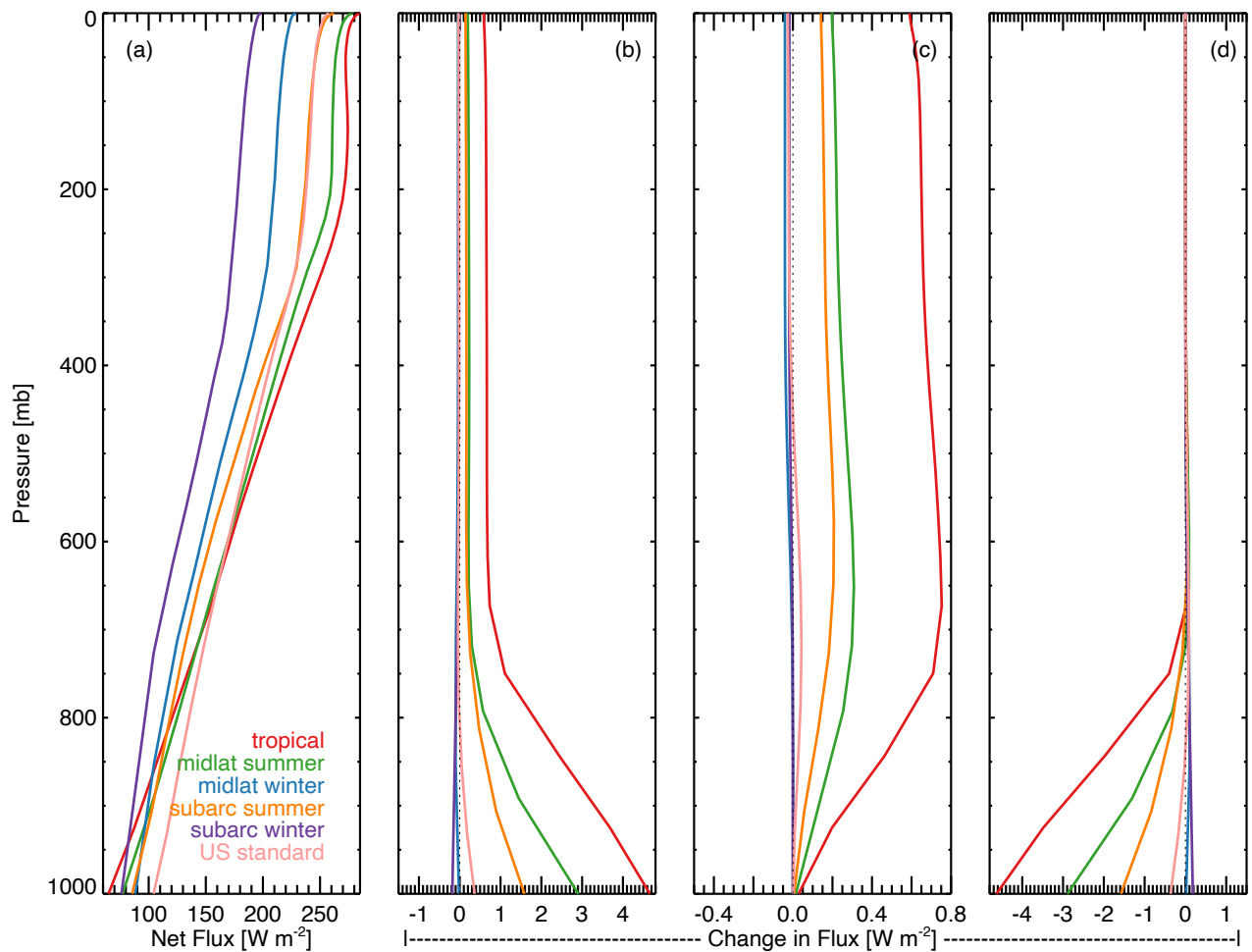
1033 **6. Impact**

1034 *6.1 Broadband fluxes and heating rates*

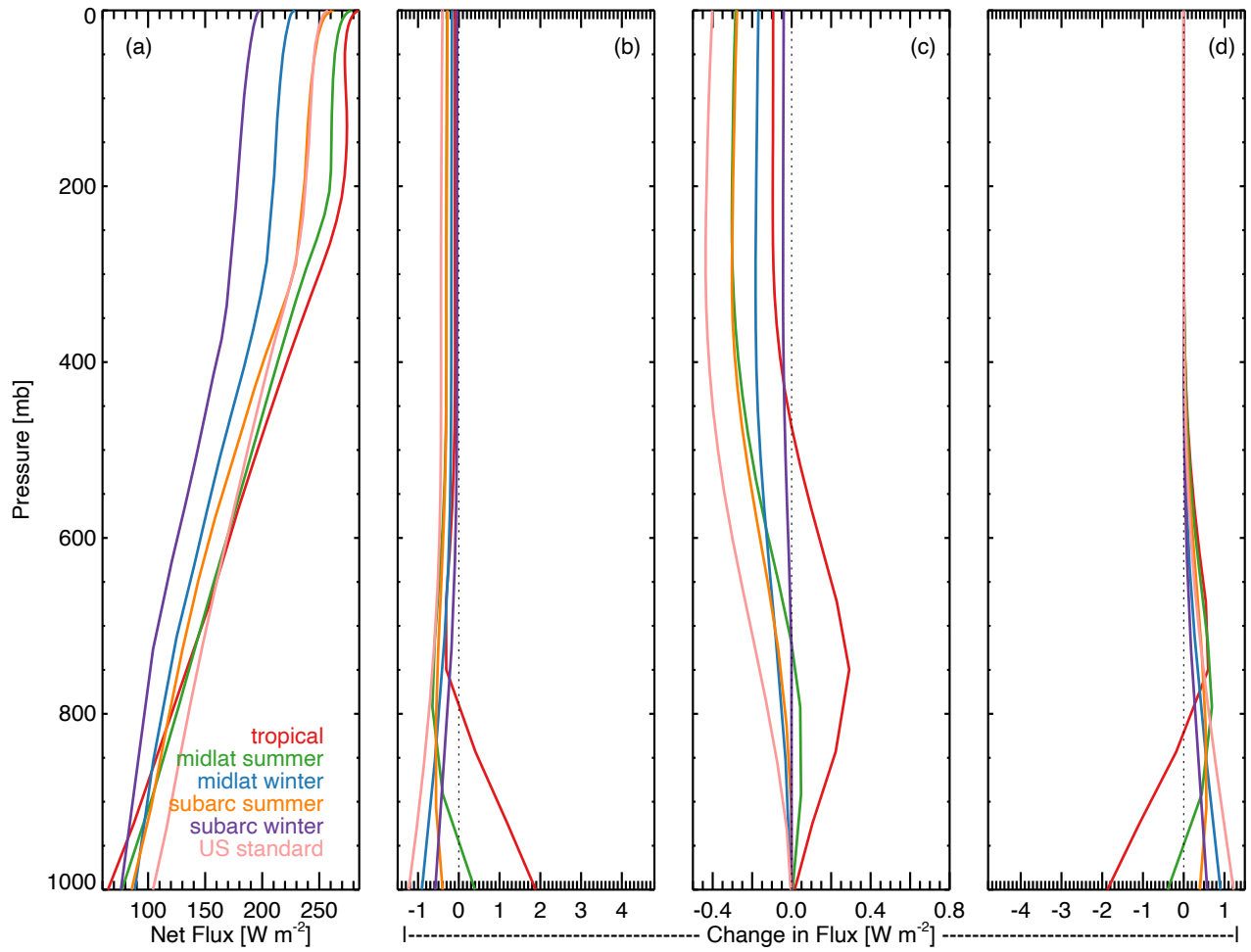
1035 The impact of the modified water vapor continuum in MT_CKD_4.2 on broadband radiative fluxes
1036 (Fig. 18) depends strongly on the moisture content of a profile. (See Table 1 for PWV values.) For
1037 dry winter profiles, the continuum modifications cause a modest decrease in upward flux and an
1038 increase in downward flux from the increased opacity due to the larger foreign continuum, which
1039 outweighs the decrease in the self continuum. The difference in downwelling flux sharply
1040 increases at ~800 mb for the tropical or summer profiles (Fig. 18d). In the tropical atmosphere, for
1041 example, the downwelling flux at the surface decreases by more than 4 W/m² as a result of the
1042 overall decrease in atmospheric opacity in the IR window caused by the 10-30% decrease in the
1043 dominant water vapor self continuum. The magnitude of the change in upwelling flux (Fig. 18c)
1044 due to the use of MT_CKD_4.2 is much smaller than for the downwelling flux since the radiating
1045 temperature of lower atmosphere, the region in which the self continuum emits radiation, does not
1046 differ too greatly from the surface temperature. Therefore, decreased absorption of surface-emitted
1047 radiation by the self continuum in MT_CKD_4.2 is partially compensated by its decreased
1048 emission of the lower atmosphere at a (typically) slightly lower temperature. Nevertheless, the
1049 upwelling radiation does increase by ~0.7 W/m² in the mid-troposphere and 0.5 W/m² at the top
1050 of the tropical atmosphere, with smaller but still notable increases for atmospheres with moderate
1051 PWV values.

1052

1053 The analysis in this study shows that the total atmospheric opacity in the infrared window is less
1054 than had previously been thought, but the exact partitioning between the water vapor continuum
1055 and aerosols, i.e. the difference between MT_CKD_4.2 and MT_CKD_4.2_closure, is quite
1056 uncertain. Fig. 19, which shows the analogous results to those in Fig. 18 for calculations using
1057 MT_CKD_4.2_closure, may better reflect the impact on fluxes resulting from this study since all
1058 sources of opacity in the infrared window are accounted for. In drier conditions the increase in
1059 atmospheric opacity in MT_CKD_4.2_closure results in an increase in downwelling flux at the
1060 surface, consistent with the change in the measurement-calculation residuals (e.g. Fig. 11) for



1061 **Fig. 18.** For six standard atmospheres: (a) longwave net flux from LBLRTM calculations using
 1062 MT_CKD_4.1.1; (b) Difference in net flux between calculations that use MT_CKD_4.2 and calculations
 1063 that use MT_CKD_4.1.1; (c) Difference in upward flux between MT_CKD_4.2 and MT_CKD_4.1.1; (d)
 1064 Difference in downward flux between MT_CKD_4.2 and MT_CKD_4.1.1.
 1065



1066 **Fig. 19.** Same as Fig. 18, but differences in (b) through (d) are for calculations that use
 1067 MT_CKD_4.2_closure and those that use MT_CKD_4.1.1.
 1068

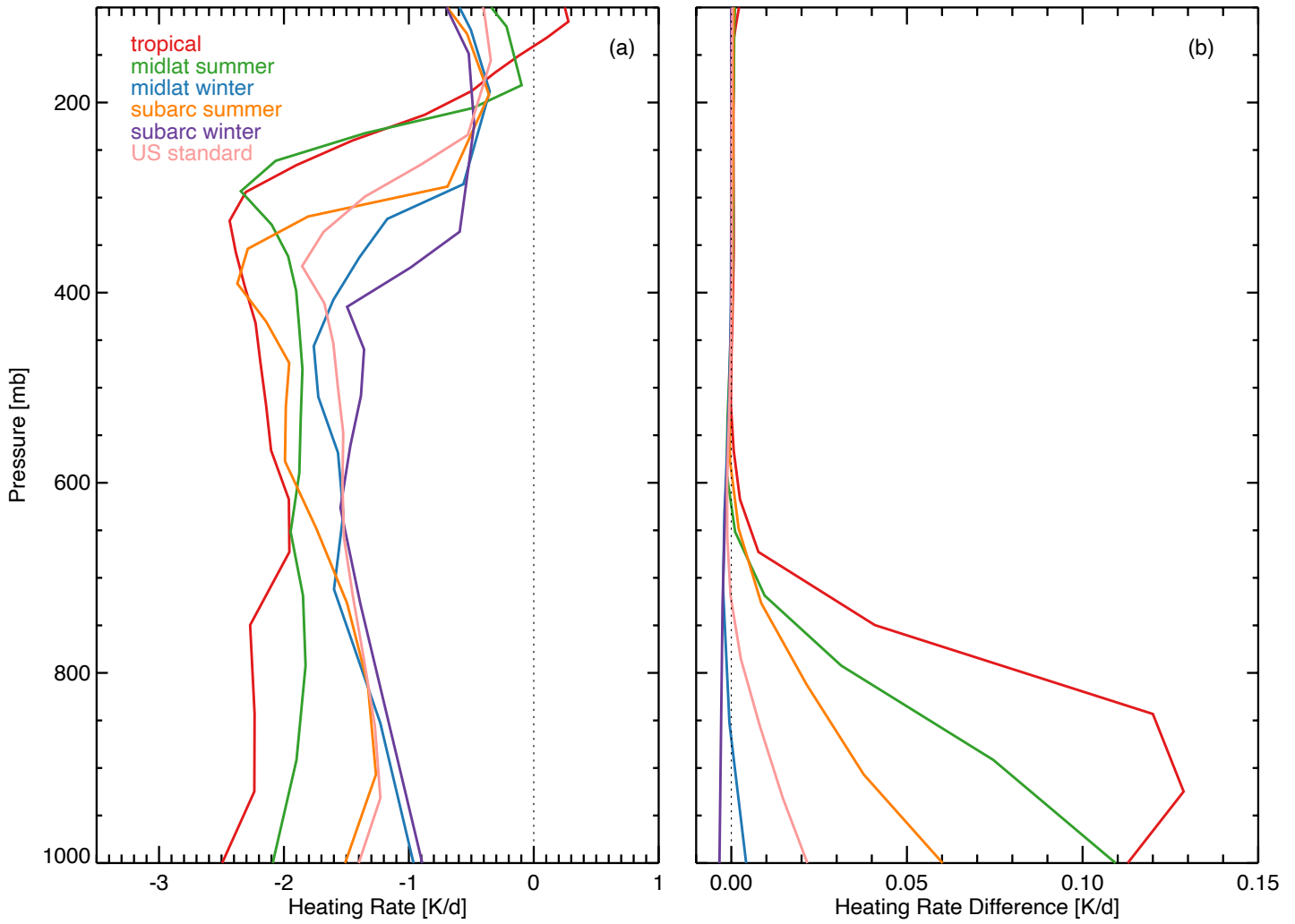
1069 similarly low PWVs. For higher PWV cases, the decreased overall absorption, driven by the
1070 decrease in the optical depth of the dominant self continuum, results in a decrease in surface
1071 downwelling flux. For upwelling flux at TOA, all cases shown in Fig. 19 show a decrease due to
1072 the continuum changes. Even for moist cases in which the magnitude of the increase in foreign
1073 continuum optical depth is less than the decrease in the self continuum, the change in foreign
1074 continuum results in an upwelling flux difference of larger magnitude since foreign continuum
1075 emission occurs higher in the atmosphere, i.e. at temperatures that differ more with respect to the
1076 surface temperature than the self continuum emission temperature. Crucially, the impact on fluxes
1077 may be very different when the aerosol properties (*e.g.* loading) differ greatly from the aerosols at
1078 the location analyzed in this study since the presumed contribution of aerosols is included in the
1079 foreign continuum in these calculations.

1080
1081 Fig. 20 shows the difference in longwave heating rates due to modifications in MT_CKD_4.2. The
1082 largest changes occur in moist atmospheres, with the heating rates increasing (less cooling) by
1083 ~5% in the lower layers of the atmospheres. Fig. S1 presents analogous results for
1084 MT_CKD_4.2_closure.

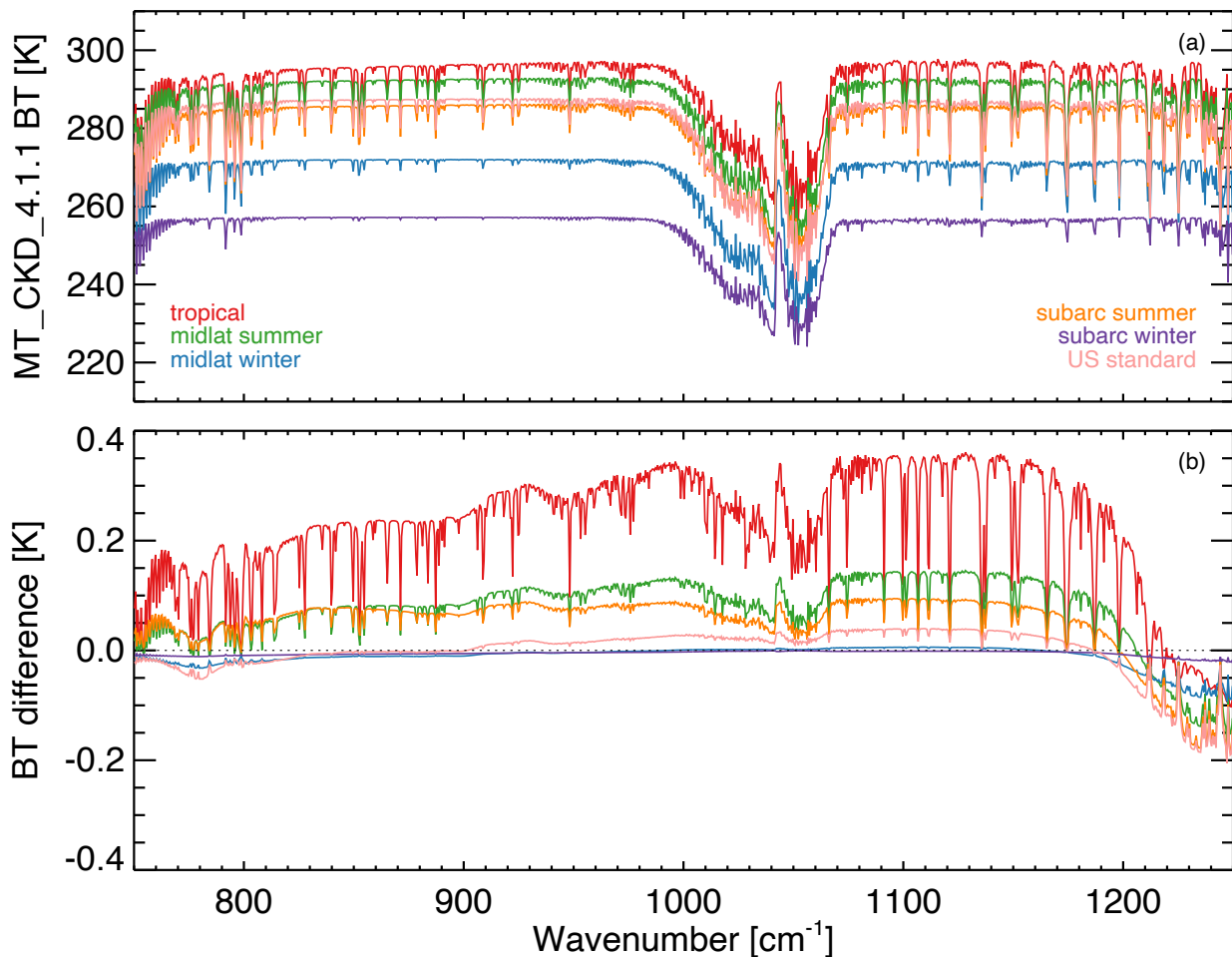
1085 1086 *6.2 Top of the atmosphere brightness temperature*

1087 Fig. 21 shows the change in the brightness temperature at the top of the atmosphere between
1088 LBLRTM calculations that use MT_CKD_4.2 and those that use MT_CKD_4.1.1. These
1089 differences increase with the PWV of the atmospheric profile, with maximum of ~+0.3 K for the
1090 tropical atmosphere, and do not show a great deal of spectral variability throughout the infrared
1091 window. This suggests that use of the new continuum version will lead to a non-trivial change in
1092 surface temperatures retrieved using satellite radiances in the infrared window. Fig. S2 provides
1093 analogous results for MT_CKD_4.2_closure. For all but the moistest of the profiles shown, the
1094 change in brightness temperature is negative due to the additional absorption provided by the
1095 aerosol assumed to be included in the foreign continuum.

1096



1097 **Fig. 20.** For six standard atmospheres: (a) longwave heating rates from LBLRTM calculations using
 1098 MT_CKD_4.1.1 and (b) difference in heating rates between calculations that use MT_CKD_4.2 and
 1099 calculations that use MT_CKD_4.1.1.
 1100



1101 **Fig. 21.** For six standard atmospheres: (a) brightness temperatures calculated with LBLRTM with
 1102 MT_CKD_4.1.1 and (b) brightness temperature differences between calculations that use MT_CKD_4.2
 1103 and calculations that use MT_CKD_4.1.1.

1104

1105 5.3 Climate considerations

1106 Since only a small fraction of the radiative forcing due to carbon dioxide and methane occurs in
 1107 the infrared window, the change in the water vapor continuum derived in this work will result in
 1108 an insignificant change in these forcings. Therefore, no relevant results are shown here.

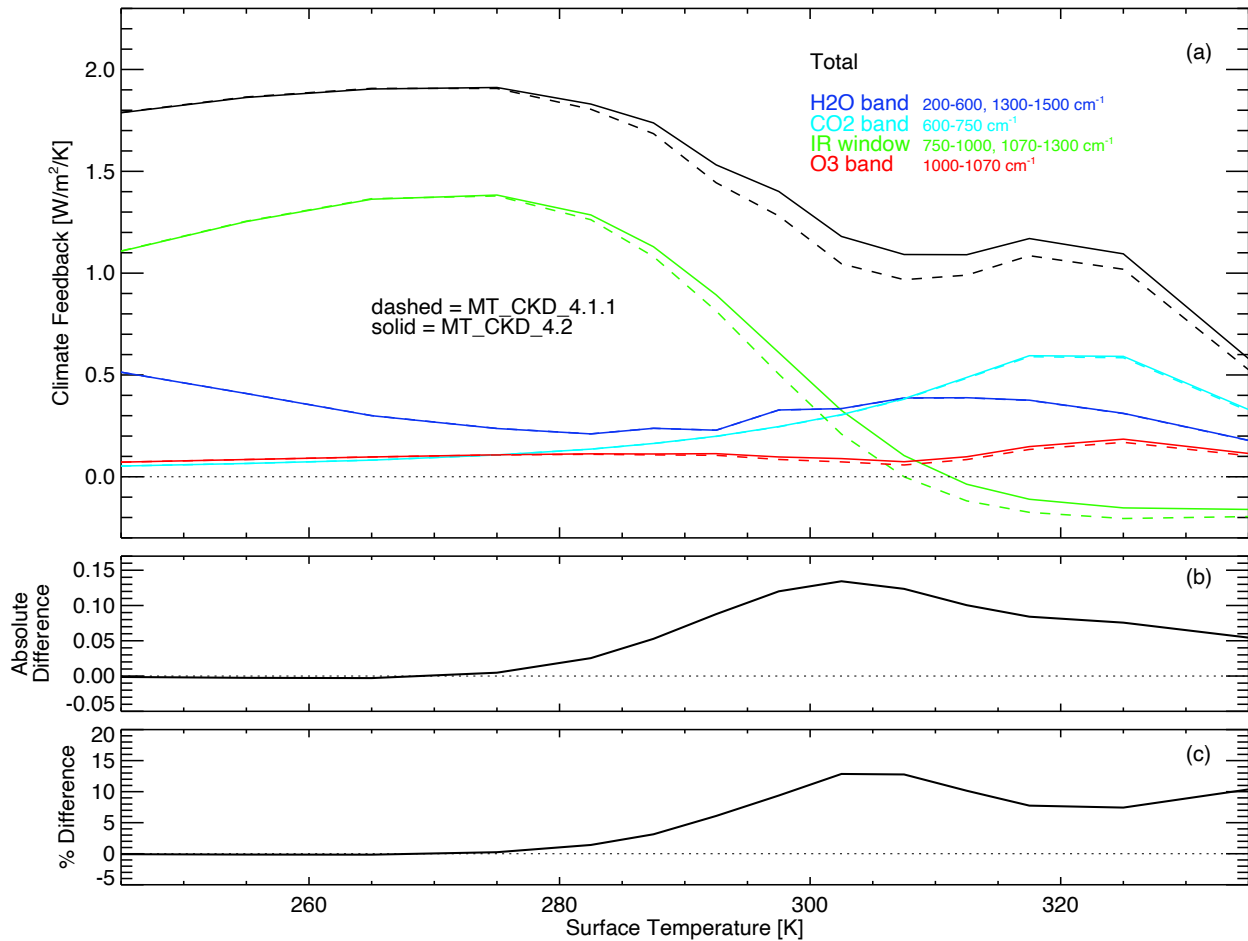
1109

1110 We assess the impact of the new continuum and resulting opacity change in the infrared window
 1111 on climate feedbacks with radiative calculations for idealized atmospheric profiles (see, e.g. Koll
 1112 and Cronin, 2018) using a range of surface temperatures from 240-340K (in 5K increments).
 1113 Atmospheric temperatures follow a moist adiabat until reaching 220K (defined as the tropopause);
 1114 temperatures above the tropopause are fixed at 220K. Relative humidity in the troposphere is 75%

1115 and carbon dioxide and ozone concentrations are based on the U.S. Standard atmosphere (ozone
1116 concentrations are zero above the tropopause and rescaled in the troposphere to ensure the same
1117 total column amount at all surface temperatures). The change in flux between consecutive surface
1118 temperatures is interpreted as the climate feedback. Fig. 22 shows this feedback as determined
1119 with the existing water vapor continuum (v4.1.1, dashed curves) and with the newly derived
1120 continuum (v4.2, solid curves). Differences are shown in the lower panels. Changes to the
1121 continuum, and the resulting decrease in atmospheric opacity in the infrared window, induce an
1122 increase in climate feedback of ~5% at current surface temperature (~290K), rising to greater than
1123 10% for a surface temperature of ~300K.

1124
1125 The colored curves in Fig. 22 show the contributions of key spectral regions to the total climate
1126 feedback. (For this figure, we have slightly expanded the spectral region defined as the window to
1127 include the entire region in which the continuum has been modified in this study.) At current Earth
1128 temperatures, the infrared window (green) is the spectral region with by far the largest climate
1129 feedback. Secondary contributions to the total climate feedback are also provided by infrared water
1130 vapor absorption bands, the CO₂ ν₂ band at 15 μm (600-750 cm⁻¹), and the main infrared ozone
1131 band at 9.6 μm (1000-1070 cm⁻¹). The climate feedback in the infrared window region decreases
1132 with surface temperature due to the increase in atmospheric opacity in moister atmospheres. This
1133 opacity increase is rapid due to the dominant role of the water vapor self continuum in the window
1134 region and its quadratic dependence on water vapor concentration. The decrease in the climate
1135 feedback in the infrared window for higher surface temperatures is partially compensated for by
1136 increases in the climate feedback in water vapor absorption bands and the CO₂ band, which has
1137 the largest contribution for surface temperatures larger than ~307K.

1138
1139 Fig. 22 shows the significant increase in climate feedback in the infrared window due to the
1140 continuum changes derived in this study. The reduced opacity in the revised water vapor
1141 continuum results in the climate feedback in the infrared window becoming negative at a
1142 temperature 3K greater than before this revision. Our calculations do not extend to sufficiently
1143 high temperatures for the climate feedback for the complete longwave region (black curve) to
1144 become negative (i.e. runaway greenhouse), but Fig. 22 suggests that the revised continuum
1145 implies that runaway greenhouse conditions will occur on Earth at a slightly higher temperature

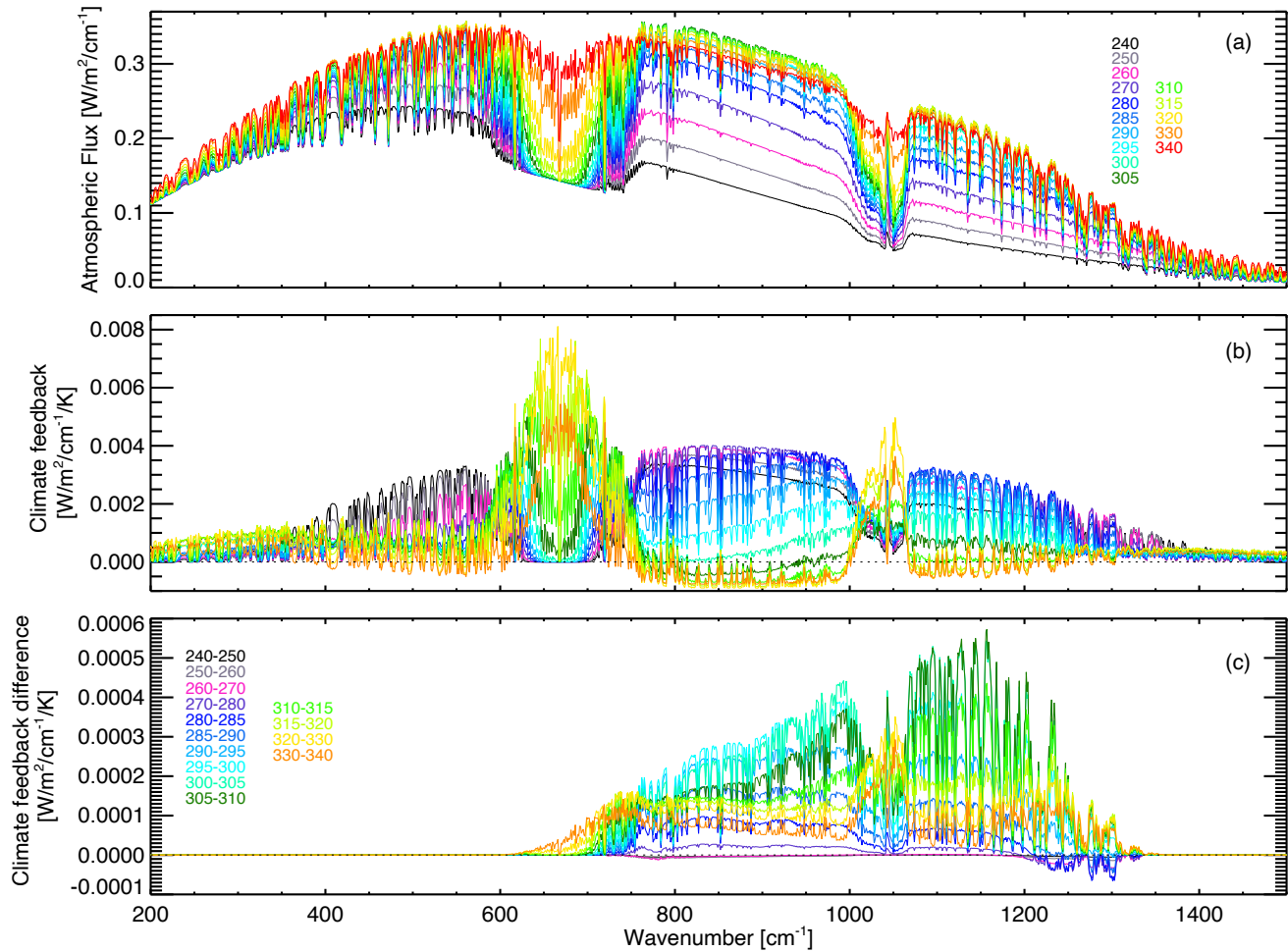


1146 **Fig 22.** As a function of surface temperature in moist adiabat profiles (as described in text), (a) climate
 1147 feedback for full longwave region (black), water vapor absorption bands (blue), CO₂ v₂ band (cyan),
 1148 infrared window (green), and ozone band (red). Solid curves use revised continuum (MT_CKD_4.2) in the
 1149 calculations while dashed curves use previous continuum (MT_CKD_4.1.1); (b) for full longwave, climate
 1150 feedback differences between calculations using MT_CKD_4.2 and MT_CKD_4.1.1; and (c) percentage
 1151 differences in climate feedback between calculations using MT_CKD_4.2 and MT_CKD_4.1.1. Climate
 1152 feedback is defined as the change in TOA flux per unit change in surface temperature.
 1153

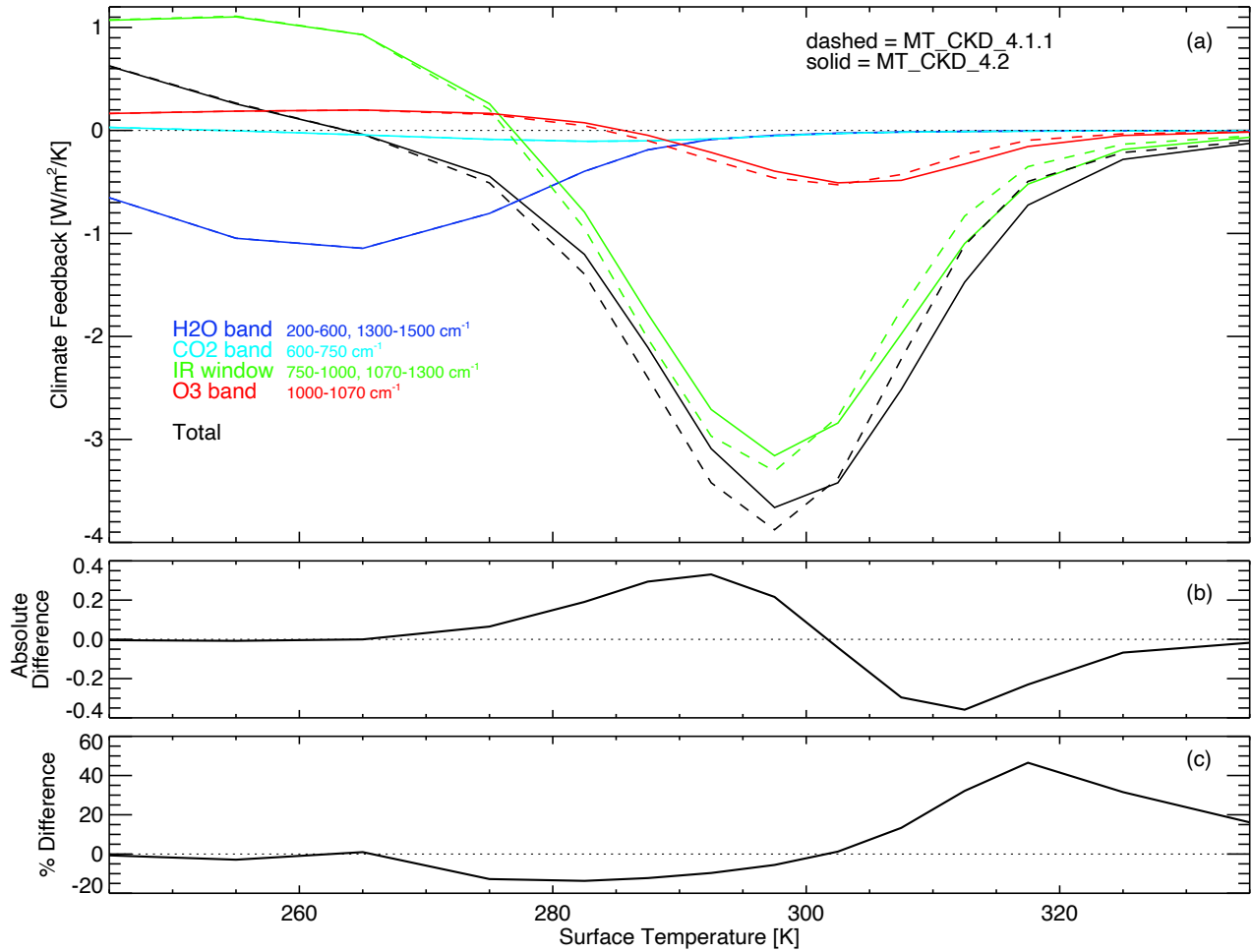
1154 than had been previously thought. (Analogous results to those presented in Fig. 22 can be seen in
1155 Fig. S3 for MT_CKD_4.2_closure.)

1156
1157 Fig. 23 shows spectrally-resolved climate feedbacks computed with MT_CKD_4.2 (panel b) and
1158 the difference with respect to MT_CKD_4.1.1 (panel c); analogous results for
1159 MT_CKD_4.2_closure are shown in Fig. S4. Since the changes to the continua decrease absorption
1160 due to the self continuum, which is the dominant source of opacity in this region, with the new
1161 continuum the climate feedback is increased throughout the vast majority of the infrared window
1162 region. The exception is in the region $1200\text{-}1300\text{ cm}^{-1}$ for low surface temperatures (i.e. lower
1163 PWV values) where, under these conditions, the increased absorption due to the revised foreign
1164 continuum can outweigh the impact of the reduced self continuum, leading to a decrease in opacity
1165 and a slight increase in climate feedback. Fig. 23c indicates that the change in climate feedback
1166 varies spectrally and with surface temperature, a result of the varying spectral behavior of the
1167 continuum changes and atmospheric opacity for the different surface temperatures. Additional
1168 discussion about the climate feedback results in Figs. 22 and 23 is provided in the supplementary
1169 material.

1170
1171 Changes resulting from the new continuum formulation to the surface net radiative flux (defined
1172 positive upwards), key to processes such as evaporation, are shown in Fig. 24 as a function of
1173 surface temperature for these moist adiabat calculations; spectral results are shown in Fig. S5.
1174 Analogous results for MT_CKD_4.2_closure are shown in Fig. S6 and Fig. S7, respectively. The
1175 results in Fig. 24 reflect a balance between the increase in upwelling surface flux with increasing
1176 surface temperature and an increase in downwelling surface flux due to the increased atmospheric
1177 temperature and water vapor loadings associated with the increased surface temperature. At low
1178 surface temperature, the low water vapor amounts lead to the former term being larger, so the
1179 “surface climate feedback” shown is positive. When the surface temperature is larger than 270K,
1180 the impact of the increase in atmospheric opacity associated with a greater surface temperature
1181 becomes increasing large, leading to a negative surface climate feedback. The magnitude of this
1182 feedback, dominated by the infrared window region, continues to increase with surface
1183 temperature until $\sim 300\text{K}$. At higher temperatures, the most opaque part of this region ($\sim 800\text{ cm}^{-1}$)
1184 has become sufficiently opaque so that its surface net flux is small and, therefore, the change in



1185 **Fig 23.** For various surface temperatures (colored curves) in moist adiabat profiles (as described in text):
 1186 (a) TOA longwave flux calculated using MT_CKD_4.2; (b) spectral behavior of climate feedback
 1187 calculated for the temperature ranges denoted on panel (c); and (c) spectral climate feedback differences
 1188 between calculations using MT_CKD_4.2 and MT_CKD_4.1.1.



1189 **Fig 24.** Similar to Fig. 22 but for the surface instead of TOA. Surface climate feedback is defined as the
1190 change in surface net flux (defined as positive upward) per unit change in surface temperature.
1191
1192 surface net flux values resulting from a change in surface temperature decreases. These spectral
1193 regions stop contributing appreciably to the surface climate feedback, and the overall magnitude
1194 starts to decrease. This trend continues as the surface temperature increases until the surface net
1195 flux approaches zero, as does the surface climate feedback.

1196
1197 The impact of the changes to the infrared window continuum is to decrease the magnitude of the
1198 surface climate feedback for lower surface temperatures, where the trend in surface climate
1199 feedback is due to the increase in surface downwelling flux due to the increased atmospheric
1200 opacity – the decrease in the self continuum slows down this trend. Conversely, for higher
1201 temperatures, the decrease in self continuum opacity decelerates the trend of the surface net flux
1202 approaching zero, thereby leading to an increase in the magnitude of the surface climate forcing.

1203
1204 For completeness, the Supplemental Materials includes analogous figures (both for MT_CKD_4.2
1205 and 4.2_closure) for the atmospheric net flux (TOA minus surface net flux) for the moist adiabat
1206 calculations, change in atmospheric net flux due to the change in surface temperature
1207 (“atmospheric climate feedback”), and changes in this feedback due to the revised water vapor
1208 continuum in the infrared window (Figs. S8-S11).

1209

1210 **7. Conclusion and discussion**

1211 This study provides a new determination of the strength of water vapor continuum absorption in
1212 the infrared atmospheric window, which, despite its importance to climate, has not been the subject
1213 of many observational studies in the last two decades. Our results are consistent with several recent
1214 analyses that indicate that the self continuum, the dominant source of atmospheric absorption in
1215 this spectral region, is too strong in MT_CKD_4.1.1. In general, the weaker self continuum derived
1216 here results in an overall increase in atmospheric transparency in the window in MT_CKD_4.2
1217 compared to MT_CKD_4.1.1. However, the transparency in atmospheres with low amounts of
1218 water vapor, which is high, may slightly decrease due to the increase in foreign continuum
1219 absorption derived in this study. These continuum changes lead to a significant decrease in
1220 downwelling longwave flux at the surface for moist atmospheres as well as a modest increase in
1221 OLR. The increased fraction of surface-leaving radiation that escapes to space leads to a notable
1222 increase (~5-10%) in the clear-sky climate feedback.

1223
1224 The diversity of the continuum values derived in previous studies is striking, and the high
1225 uncertainty of some of the continuum values we have derived means that our study cannot resolve
1226 all remaining uncertainties of significance to Earth’s radiative budget and climate. This is
1227 especially the case for the foreign continuum and the temperature dependence of the self
1228 continuum, but also for the self continuum in certain spectral regions (e.g. 1150-1200 cm^{-1}). This
1229 reality points to the need for further accurate laboratory studies of the water vapor continuum in
1230 the atmospheric window. Within the last year, an important step in this direction has occurred.
1231 Motivated by a presentation of preliminary results from this study (Mlawer et al., 2022), the
1232 Campargue group at the University of Grenoble Alpes undertook a measurement of the self
1233 continuum at $\sim 1185 \text{ cm}^{-1}$ using the accurate technique of optical feedback cavity ring down

1234 spectroscopy. The results of this study (Fournier et al., 2023; F23) are consistent with our result
1235 that there is a need for a significant reduction in the strength of the MT_CKD_4.1.1 self continuum
1236 in this region, although the decrease derived in our study is greater than in F23. The two results
1237 agree within the uncertainties associated with our determination of the self continuum in this
1238 region. Measurements of the self continuum were performed in F23 over a limited range of
1239 temperatures (296-308 K), which resulted in the determination that the temperature dependence is
1240 much weaker than the value we have implemented in MT_CKD_4.2. Given that our study
1241 determined that the self continuum temperature dependence could assume a wide range of values
1242 while still allowing radiative closure with AERI measurements, this is not surprising. There is a
1243 clear need for additional accurate laboratory studies of the self continuum across the full
1244 atmospheric window, as well as its temperature dependence and the strength of foreign continuum
1245 absorption.

1246
1247 The foreign continuum analysis in this study also demonstrates the need for further laboratory
1248 studies of this source of atmospheric absorption. In this study, we posit that our derivation of
1249 foreign continuum absorption includes a contribution from aerosols and determine the spectrally
1250 dependent fraction of the absorption due to the foreign continuum vs. aerosols through a highly
1251 speculative approach. Despite the resulting substantial uncertainty inherent our methodology, our
1252 results point out the possibly important role that aerosol absorption may play in the longwave
1253 radiative budget, which we hope will prompt further study.

1254
1255

1256 **Appendix 1**

1257 The method to estimate the “adjusted” self continuum values shown in Fig. 4d for three previous
1258 field studies is described here. Using the SGP dataset described in Section 3, we retrieved self
1259 continuum values (see section 4.2 for the description of the methodology) using the
1260 MT_CKD_4.1.1+BL foreign continuum. For our reconsideration of the Turner et al. (2004) study,
1261 we used the entire dataset to estimate the change in derived self continuum values due to the
1262 modified foreign continuum, while for the tropical analyses upon which CKD_2.1 was based
1263 (Westwater et al., 1995; Han et al., 1997) we used only the most moist cases in the SGP dataset.
1264 These revised self continuum values are shown in Fig. 4d as MT_CKD_1.0_adj and CKD_2.1_adj,
1265 respectively. Also shown in this figure are the self continuum values derived in a field study by
1266 Taylor et al. (2003), which assumed the CKD_2.4 foreign continuum, and corresponding self
1267 continuum values that are estimated as the values that would have been obtained had the larger
1268 MT_CKD_4.1.1+BL foreign continuum values been assumed instead (denoted as “Taylor_adj”).

1269

1270 **Appendix 2**

1271 Based on a) the foreign continuum value at 980 cm^{-1} from a revised line shape fit (similar to the
1272 one used to derive MT_CKD_1.0 as described in Mlawer et al., 2012) applied to the foreign
1273 continuum coefficients in MT_CKD_4.1.1 from $500\text{-}800\text{ cm}^{-1}$ and b) the value of the foreign
1274 continuum at 980 cm^{-1} in MT_CKD_4.2_closure, we estimate that the actual foreign continuum is
1275 a little more than half of the retrieved foreign continuum at 980 cm^{-1} , and assume that aerosols are
1276 responsible for the remaining fraction. This split between foreign continuum and aerosol is
1277 weighted more to the foreign continuum than is implied by Fig. 15, but is within the uncertainty
1278 of the aerosol optical depth estimates in panel b of that figure. The first step in the procedure to
1279 account for the estimated impact of aerosols on the derived spectral foreign continuum coefficients
1280 is to compute the spectral fraction of the derived continuum due to aerosol optical depths. To do
1281 this, the spectral dependence of the aerosol optical depth is assumed to be given by a derived
1282 Angstrom exponent of -0.647 while the combined foreign and aerosol optical depth is given by
1283 MT_CKD_4.2_closure. Using this ratio, the estimated aerosol contribution is removed from the
1284 derived foreign continuum coefficients, yielding an estimate of the actual foreign continuum
1285 coefficients (i.e. with aerosol removed). It is important to note that since no coefficients were
1286 derived from $990\text{-}1070\text{ cm}^{-1}$, this gap remains in these estimated pure continuum coefficients.

1287 These coefficients are then used as constraints in a new fit of the same line shape formalism that
1288 was used to derive MT_CKD_1.0. The new fit is aimed at providing values for the foreign
1289 continuum in the gap as well as in neighboring spectral regions that are impacted greatly by
1290 aerosols (given our assumption) and, therefore, the derived foreign continuum coefficients in those
1291 regions cannot be considered very definitive (e.g. 1080-1150 cm^{-1}). The main priorities in the
1292 fitting effort are to match the following properties of the constraining foreign continuum
1293 coefficients: a) the overall slope of the coefficients from 800-980 cm^{-1} and b) the coefficient
1294 values in spectral regions closest to the gap in which the actual foreign continuum value are thought
1295 to be responsible for more than 60% of the AERI-derived foreign continuum coefficients (960-
1296 980 cm^{-1} and 1220-1230 cm^{-1}). The continuum coefficients resulting from this fit are the final
1297 foreign continuum coefficients in the targeted spectral region; in neighboring spectral regions the
1298 coefficients from the fit are smoothly merged with the constraining coefficients (i.e. AERI-
1299 derived), resulting in the final foreign water vapor coefficients from this AERI analysis (780 -
1300 1250 cm^{-1}). In spectral regions just outside of this range, these coefficients are transitioned into
1301 the existing MT_CKD_4.1.1 foreign continuum coefficients in spectral regions ($< 600 \text{ cm}^{-1}$, $>$
1302 1400 cm^{-1}) in which the coefficients have been determined in previous observation-based analyses.
1303
1304

1305 **Acknowledgements**

1306 The primary support for this project at AER was provided by Atmospheric Systems Research
1307 (ASR) program of the U.S. Department of Energy under contract number DE-SC0018296.
1308 Additional support for the analysis and dissemination of the results were provided by the NASA
1309 U.S. Participating Investigator program under contract number 80NSSC21K1038 and the National
1310 Science Foundation under award number 1916927. Support at NOAA was provided by ASR
1311 contract 89243019SSC000034. We thank the DOE Atmospheric Radiation Measurement program
1312 for the observations upon which this study is based and for their excellent data archive. AER
1313 authors are indebted to Karen Cady-Pereira, Matt Alvarado, and Rick Pernak for helpful advice.
1314 Part of this research was carried out at the Jet Propulsion Laboratory, California Institute of
1315 Technology, under a contract with NASA (80NM0018D0004).

1316

1317 **Open Research**

1318 *Data availability.*

1319 All SGP and MAO observations used in this study were obtained from <https://www.arm.gov/data>.
1320 The LBLRTM radiative transfer model can be accessed from <https://github.com/AER-RC/LBLRTM>
1321 and the MT_CKD continuum model from https://github.com/AER-RC/MT_CKD.
1322 The LBLRTM input files derived from ARM observations that are used in this study can be found
1323 in a tar file that can be downloaded from Zenodo (<https://zenodo.org/records/10909710>). The
1324 Zenodo file also contains all aerosol-related data used in our analysis, as well as the code (Python)
1325 used to retrieve the self and foreign continuum coefficients and the self continuum temperature
1326 exponents from the measurement-calculation residuals. Additional supporting information is also
1327 available in this tar file. All analysis and plots were executed using Python 3.9.7 and IDL Version
1328 8.4.

1329

1330 **Supporting information**

1331 Additional text and data can be found in *mlawer_ir-window_supporting_information.pdf*.

1332

1333

1334 **References**

- 1335 Anderson, G. P., Clough, S. A., Kneizys, F. X., Chetwynd, J. H., & Shettle, E. P. (1986). AFGL
1336 atmospheric constituent profiles (0.120 km). (No. AFGL-TR-86-0110). Air Force Geophysics
1337 Lab, Hanscom, AFB, MA. Retrieved from <http://www.dtic.mil/docs/citations/ADA175173>
1338
- 1339 Baranov, Y.I., Lafferty W.J., Ma Q., & Tipping R.H. (2008). Water vapor continuum absorption
1340 in the 800-1250 cm^{-1} spectral region at temperatures from 311 to 363K. *J Quant Spectrosc Radiat*
1341 *Transf.*, 109, 2291–2302.
1342
- 1343 Baranov, Y.I & Lafferty W.J. (2012). The water vapor self- and water–nitrogen continuum
1344 absorption in the 1000 and 2500 cm^{-1} atmospheric windows. *Philos Trans R Soc A*, 370, 2578–
1345 2589.
1346
- 1347 Burch, D.E. (1982). Continuum absorption by H₂O. *AFGL-TR-81-0300*. 46 pp. Air Force
1348 Geophys. Lab., Hanscom AFB, MA. <http://dx.doi.org/10.1117/12.931899>
1349
- 1350 Burch, D.E. & Alt, R.L. (1984). Continuum absorption by H₂O in the 700-1200 cm^{-1} and 2400-
1351 2800 cm^{-1} windows. *AFGL-TR-84-0128*, 32 pp., Air Force Geophysics. Lab., Hanscom AFB, MA.
1352
- 1353 Cadeddu, M. P., Liljegren, J. C., & Turner, D. D. (2013). The Atmospheric radiation measurement
1354 (ARM) program network of microwave radiometers: instrumentation, data, and retrievals. *Atmos.*
1355 *Meas. Tech.*, 6, 2359–2372. <https://doi.org/10.5194/amt-6-2359-2013>
1356
- 1357 Clough, S.A., Kneizys, F.X., & Davies, R.W. (1989). Line shape and the water vapor continuum.
1358 *Atmos. Res.*, 23, 229. [https://doi.org/10.1016/0169-8095\(89\)90020-3](https://doi.org/10.1016/0169-8095(89)90020-3)
1359
- 1360 Clough, S.A., Shephard, M.W., Mlawer, E.J., Delamere, J.S., Iacono, M.J., Cady-Pereira, K.,
1361 Boukabara, S., & Brown, P.D (2005). Atmospheric radiative transfer modeling: A summary of the
1362 AER codes. *J. Quant. Spectrosc. Radiative Trans.*, 91, 233-244.
1363
- 1364 Cormier J.G., Hodges J.T., & Drummond, J.R. (2005). Infrared water vapour continuum
1365 absorption at atmospheric temperatures. *J. Chem. Phys.*, 122:114309. <http://doi.org/10.1063/1.1862623>
1366
1367
- 1368 Cormier, J.G, Ciurylo, R., & Drummond, J.R. (2002). Cavity ringdown spectroscopy
1369 measurements of the infrared water vapor continuum. *J. Chem. Phys.*, 116, 1030.
1370
- 1371 Delamere, J.S., Clough, S.A., Payne, V., Mlawer, E.J., Turner, D.D., & R. Gamache (2010). A far-
1372 infrared radiative closure study in the Arctic: Application to water vapor. *J. Geophys. Res.*, 115,
1373 D17106. doi:10.1029/2009JD012968
1374
- 1375 Dubovik, O. & King, M.D. (2000). A flexible inversion algorithm for retrieval of aerosol optical
1376 properties from Sun and sky radiance measurements. *J. Geophys. Res.*, 105, 20,673-20,696.
1377

1378 Feng, J., Paynter, D., & Menzel, R. (2023). How a stable greenhouse effect on Earth is maintained
1379 under global warming. *Journal of Geophysical Research: Atmospheres*, 128, e2022JD038124.
1380 <https://doi.org/10.1029/2022JD038124>
1381

1382 Fournier, Q., Kassi, S., Mondelain, D., Fleurbaey, H., Georges, R., & Campargue, A. (2024), The
1383 water vapor self-continuum absorption at 8.45 μm by optical feedback cavity ring down
1384 spectroscopy. *J. Quant. Spectr. Rad. Trans.*, 315. <http://dx.doi.org/10.2139/ssrn.4607109>
1385

1386 Fu, D., Worden, J.R., Liu, X., Kulawik, S.S., Bowman, K.W. & Natraj, V. (2013). Characterization
1387 of ozone profiles derived from Aura TES and OMI radiances. *Atmos. Chem.*
1388 *Phys.*, 13(6), 3445–3462. doi:10.5194/acp-13-3445-2013
1389

1390 Han, Y., Shaw, J.A., Churnside, J.H., Brown, P.D., & Clough, S.A. (1997). Infrared spectral
1391 measurements in the tropical Pacific atmosphere. *J. Geophys. Res.*, 102, 4353-4356.
1392

1393 Harries, J., Carli, B., Rizzi, R., Serio, C., Mlynyczak, M., Palchetti, L., et al. (2008), The far-infrared
1394 Earth, *Rev. Geophys.*, 46, RG4004. doi:10.1029/2007RG000233
1395

1396 Jeevanjee, N., Koll, D. D., & Lutsko, N. (2021). “Simpson’s law” and the spectral cancellation of
1397 climate feedbacks. *Geophysical Research Letters*, 48(14), e2021GL093699.
1398 <https://doi.org/10.1029/2021gl093699>
1399

1400 Koll, D. D., Jeevanjee, N., & Lutsko, N. J. (2023). An analytic model for the clear-sky longwave
1401 feedback. *Journal of the Atmospheric Sciences*, 80(8), 1923-1951.
1402

1403 Koll, D. D., & Cronin, T. W. (2018). Earth’s outgoing longwave radiation linear due to H₂O
1404 greenhouse effect. *Proceedings of the National Academy of Sciences*, 115(41), 10293–10298.
1405 <https://doi.org/10.1073/pnas.1809868115>
1406

1407 Knuteson, R.O, Revercomb. H.E., Best, F.A., Ciganovich, N.C., Dedecker, R.G., Dirkx, T.P., et
1408 al. (2004a) Atmospheric Emitted Radiance Interferometer. Part I: Instrument design. *J. Atmos.*
1409 *Oceanic Technol.*, **21**, 1763-1776. <https://doi.org/10.1175/JTECH-1662.1>
1410

1411 Knuteson, R.O, Revercomb. H.E., Best, F.A., Ciganovich, N.C., Dedecker, R.G., Dirkx, T.P., et
1412 al. (2004b): Atmospheric Emitted Radiance Interferometer. Part II: Instrument performance. *J.*
1413 *Atmos. Oceanic Technol.*, **21**, 1777-1789. <https://doi.org/10.1175/JTECH-1663.1>
1414

1415 McKim, B. A., Jeevanjee, N., & Vallis, G. K. (2021). Joint dependence of longwave feedback on
1416 surface temperature and relative humidity. *Geophysical Research Letters*, 48(18),
1417 e2021GL094074. <https://doi.org/10.1029/2021gl094074>
1418

1419 Martin S.T., Artaxo, P., Machado, L., Manzi, A.O., Souza, R.A., Schumacher, C. et al. (2016). The
1420 Green Ocean Amazon Experiment (GoAmazon2014/5) Observes Pollution Affecting Gases,
1421 Aerosols, Clouds, and Rainfall over the Rain Forest. *Bulletin of the American Meteorological*
1422 *Society*, 98(5), 10.1175/bams-d-15-00221.1
1423

1424 Malm, W. C., Sislerm J. F., Huffmann, D., Eldred, R. A., & Cahill, T. A. (1994). Spatial and
1425 seasonal trends in particle concentration and optical extinction in the United States. *J. Geophys.*
1426 *Res.*, 99, 1347–1370. <https://doi.org/10.1029/93JD02916>
1427

1428 Mlawer, E.J. & Turner, D.D. (2016). Spectral radiation measurements and analysis in the ARM
1429 program. *Meteorol Monogr*, 57 14.1-14.17. doi:10.1175/AMSMONOGRAPHS-D-15-0027.1
1430

1431 Mlawer, E.J., Cady-Pereira, K.E., Mascio, J., & Gordon, I.E. (2023). The inclusion of the
1432 MT_CKD water vapor continuum model in the HITRAN molecular spectroscopic database. *J.*
1433 *Quant. Spectr. Rad. Trans.*, 306. <https://doi.org/10.1016/j.jqsrt.2023.108645>
1434

1435 Mlawer, E.J., Payne, V.H., Moncet. J.-L., Delamere, J.S., Alvarado, M.J., Tobin, D.C (2012).
1436 Development and recent evaluation of the MT_CKD model of continuum absorption. *Philos Trans*
1437 *R Soc A*, 370, 2520–56. doi:10.1098/rsta. 2011.0295
1438

1439 Mlawer, E.J., Taubnam, S.J., Brown, P.D., Iacono, M.J., and Clough, S.A. (1997). RRTM, a
1440 validated correlated-k model for the longwave. *J. Geophys. Res.*, 102, 16663-16682.
1441

1442 Mlawer, E.J., Turner, D.D., Paine, S.N., Palchetti, L., Bianchini, G., Payne, V.H., et al. (2019).
1443 Analysis of water vapor absorption in the far-infrared and submillimeter regions using surface
1444 radiometric measurements from extremely dry locations. *J Geophys Res Atmos*, 124,8134–60.
1445 doi:10.1029/2018JD029508
1446

1447 Otsu, N. (1979). A threshold selection method from gray-level histograms. *IEEE Transactions on*
1448 *Systems, Man, and Cybernetics*. 9 (1): 62–66. [doi:10.1109/TSMC.1979.4310076](https://doi.org/10.1109/TSMC.1979.4310076).
1449 [S2CID 15326934](https://doi.org/10.1109/TSMC.1979.4310076)
1450

1451 Randles, C. A., da Silva, A. M., Buchard, V., Colarco, P. R., Darmenov, A., Govindaraju, R., et
1452 al. (2017). The MERRA-2 Aerosol Reanalysis, 1980 onward. Part I: System description and data
1453 assimilation evaluation. *J. Climate*, 30(17), 6823–6850. [https://doi.org/10.1175/JCLI-D-16-](https://doi.org/10.1175/JCLI-D-16-0613.1)
1454 [0613.1](https://doi.org/10.1175/JCLI-D-16-0613.1)
1455

1456 Revercomb, H.E., Buijs, H., Howell, H.B., LaPorte, D.D., Smith, W.L., and Sromovsky, L.A.
1457 (1988). Radiometric calibration of IR Fourier transform spectrometers: Solution to a problem with
1458 the high-resolution interferometer sounder. *Appl. Opt.*, 27, 3210-3218.
1459

1460 Revercomb, H.E., Turner, D.D., Tobin, D.C., Knuteson, R.O., Feltz, W.F., Barnard, J. et al. (2003)
1461 The Atmospheric Radiation Measurement Program's water vapor intensive observation periods:
1462 overview, initial accomplishments, and future challenges. *Bull. Amer. Meteor. Soc.*, **84**, 217-236
1463

1464 Seeley, J. T., & Jeevanjee, N. (2021). H₂O windows and CO₂ radiator fins: A clear-sky explanation
1465 for the peak in equilibrium climate sensitivity. *Geophysical Research Letters*, 48(4),
1466 e2020GL089609. <https://doi.org/10.1029/2020gl089609>
1467

1468 Shephard, M.W., Goldman, A., Clough, S.A., Mlawer, E.J. (2003) Spectroscopic improvements
 1469 providing evidence of formic acid in AERI-LBLRTM validation spectra. *J. Quant. Spectr. Rad.*
 1470 *Trans.*, 82, 383-390. [https://doi.org/10.1016/S0022-4073\(03\)00164-X](https://doi.org/10.1016/S0022-4073(03)00164-X).
 1471

1472 Simpson, G. (1928). Some studies in terrestrial radiation. *Memoirs of the Royal Meteorological*
 1473 *Society*, 2(16), 69–95.
 1474

1475 Sisterson, D.L, Peppler, R.A., Cress, T.S., Lamb, P.J., and Turner, D.D. (2016). The ARM
 1476 Southern Great Plains (SGP) site. *The Atmospheric Radiation Measurement Program: The First*
 1477 *20 Years*, *Meteor. Monograph. Amer. Meteor. Soc.*, 57, 6.1-6.14,
 1478 DOI:10.1175/AMSMONOGRAPHS-D-16-0004.1
 1479

1480 Slingo, A. and Webb, M.J. (1997), The spectral signature of global warming. *Quarterly Journal*
 1481 *of the Royal Meteorological Society*, 123(538), 293–307. <https://doi.org/10.1002/qj.49712353803>
 1482

1483 Taylor, J.P., Newman, S.M., Hewison, T.J., & McGrath, A. (2003). Water vapour line and
 1484 continuum absorption in the thermal infrared – reconciling models and observations
 1485 *Quart. J. Roy. Meteorol. Soc.*, 129 (2003),2949-2969. [10.1256/qj.03.08](https://doi.org/10.1256/qj.03.08)
 1486

1487 Turner, DD., 2003: Microphysical properties of single and mixed-phase Arctic clouds derived
 1488 from ground-based AERI observations. Ph.D. Dissertation, University of Wisconsin-Madison, 167
 1489 pp. Available from <https://search.library.wisc.edu/catalog/999951770902121>
 1490

1491 Turner, D.D. (2005). Arctic mixed-phase cloud properties from AERI-lidar observations:
 1492 Algorithm and results from SHEBA. *J. Appl. Meteor.*, 44, 427-444.
 1493

1494 Turner, D.D. (2008). Ground-based retrievals of optical depth, effective radius, and composition
 1495 of airborne mineral dust above the Sahel. *J. Geophys. Res.*, 113, E00E03,
 1496 doi:10.1029/2008JD010054
 1497

1498 Turner, D.D., Tobin, D.C., Clough, S.A., Brown, P.D., Ellingson, R.G., Mlawer, E.J. et al. (2004).
 1499 The QME AERI LBLRTM: A closure experiment for downwelling high spectral resolution
 1500 infrared radiance. *J. Atmos. Sci.*, 61, 2657-2675.
 1501

1502 Turner, D.D. & Blumberg, W.G. (2019). Improvements to the AERIOe thermodynamic profile
 1503 retrieval algorithm. *IEEE Selected Topics Appl. Earth Obs. Remote Sens.*, 12, 1339-1354,
 1504 doi:10.1109/JSTARS.2018.2874968
 1505

1506 Turner, D.D. & Ellingson, R.G. Eds., 2016: *The Atmospheric Radiation Measurement (ARM)*
 1507 *Program: The First 20 Years*. Meteor. Monograph, 57, American Meteorological Society
 1508

1509 Turner, D. D. & Löhnert, U. (2014). Information content and uncertainties in thermodynamic
 1510 profiles and liquid cloud properties retrieved from the ground-based Atmospheric Emitted
 1511 Radiance Interferometer (AERI). *J. Appl. Meteor. Climatol.*, 53, 752-771, doi:10.1175/JAMC-D-
 1512 13-0126.1
 1513

1514 Turner, D.D. & Löhnert, U. (2021). Ground-based temperature and humidity profiling: Combining
 1515 active and passive remote sensors. *Atmos. Meas. Technol.*, 14, 3033-3048, doi:10.5194/amt-14-
 1516 3033-2021

1517

1518 Turner, D.D. & Mlawer, E.J. (2010). Radiative heating in underexplored bands campaigns
 1519 (RHUBC). *Bull. Amer. Meteor. Soc.*, 91, 911-923. doi:10.1175/2010BAMS2904.1.

1520

1521 Turner, D.D., Lesht, B.M. Clough, S.A., Liljegren, J.C., Revercomb, H.E., & Tobin, D.C. (2003).
 1522 Dry bias and variability in Vaisala radiosondes: The ARM experience. *J. Atmos. Oceanic Technol.*,
 1523 20, 117-132.

1524

1525 Turner, D.D., Mlawer, E.J. & H.E. Revercomb (2016). Water vapor observations in the ARM
 1526 program. *The Atmospheric Radiation Measurement Program: The First 20 Years*. Meteor.
 1527 Monograph, 57, Amer. Meteor. Soc., 13.1-13.18, doi:10.1175/AMSMONOGRAPHIS-D-15-
 1528 0025.1

1529

1530 Wang, J., Cole, H.L., Carlson, D.J., Miller, E.R. & Beirle, K. (2002). Corrections of humidity
 1531 measurement errors from the Vaisala RS80 radiosonde – application to TOGA COARE data. *J.*
 1532 *Atmos. Oceanic Technol.*, 19, 981-1002

1533

1534 Wargan, K., Labow, G., Frith, S., Pawson, S., Livesey, N., & Partyka, G. (2017). Evaluation of
 1535 the ozone fields in NASA's MERRA-2 reanalysis. *Journal of Climate*, 30, 2961–2988.
 1536 <https://doi.org/10.1175/JCLI-D-16-0699.1>

1537

1538 Westwater, E., Churnside, J., Shaw, J., Snider, J.B., Gage, K.S., Han, Y., Ecklund, W. et al. (1995).
 1539 Ground-based remote sensor observations during the PROBE experiment in the tropical western
 1540 Pacific. 882 - 886 vol.2. 10.1109/IGARSS.1995.521086

1541

1542 Worden, H.M., Logan, J.A., Worden, J.R., Beer, R., Bowman, K., Clough, S.A. et al. (2007).
 1543 Comparisons of Tropospheric Emission Spectrometer (TES) ozone profiles to ozonesondes:
 1544 Methods and initial results, *J. Geophys. Res.*, 112, D03309. doi:10.1029/2006JD007258

1545